NASA/CR-2005-213252

A Prototype Actuator Concept For Membrane Boundary Vibration Control

Micah J. Solter
The George Washington University
The School of Engineering and Applied Science
Langley Research Center, Hampton, Virginia

February 2005

The NASA STI Program Office . . . in Profile

Since its founding, NASA has been dedicated to the advancement of aeronautics and space science. The NASA Scientific and Technical Information (STI) Program Office plays a key part in helping NASA maintain this important role.

The NASA STI Program Office is operated by Langley Research Center, the lead center for NASA's scientific and technical information. The NASA STI Program Office provides access to the NASA STI Database, the largest collection of aeronautical and space science STI in the world. The Program Office is also NASA's institutional mechanism for disseminating the results of its research and development activities. These results are published by NASA in the NASA STI Report Series, which includes the following report types:

- TECHNICAL PUBLICATION. Reports of completed research or a major significant phase of research that present the results of NASA programs and include extensive data or theoretical analysis. Includes compilations of significant scientific and technical data and information deemed to be of continuing reference value. NASA counterpart of peer-reviewed formal professional papers, but having less stringent limitations on manuscript length and extent of graphic presentations.

- TECHNICAL MEMORANDUM. Scientific and technical findings that are preliminary or of specialized interest, e.g., quick release reports, working papers, and bibliographies that contain minimal annotation. Does not contain extensive analysis.

- CONTRACTOR REPORT. Scientific and technical findings by NASA-sponsored contractors and grantees.

- CONFERENCE PUBLICATION. Collected papers from scientific and technical conferences, symposia, seminars, or other meetings sponsored or co-sponsored by NASA.

- SPECIAL PUBLICATION. Scientific, technical, or historical information from NASA programs, projects, and missions, often concerned with subjects having substantial public interest.

- TECHNICAL TRANSLATION. English-language translations of foreign scientific and technical material pertinent to NASA's mission.

Specialized services that complement the STI Program Office's diverse offerings include creating custom thesauri, building customized databases, organizing and publishing research results ... even providing videos.

For more information about the NASA STI Program Office, see the following:

- Access the NASA STI Program Home Page at ***http://www.sti.nasa.gov***

- E-mail your question via the Internet to help@sti.nasa.gov

- Fax your question to the NASA STI Help Desk at (301) 621-0134

- Phone the NASA STI Help Desk at (301) 621-0390

- Write to:
  NASA STI Help Desk
  NASA Center for AeroSpace Information
  7121 Standard Drive
  Hanover, MD 21076-1320

NASA/CR-2005-213252

A Prototype Actuator Concept For Membrane Boundary Vibration Control

Micah J. Solter
The George Washington University
The School of Engineering and Applied Science
Langley Research Center, Hampton, Virginia

National Aeronautics and
Space Administration

Langley Research Center
Hampton, Virginia 23681-2199

Prepared for Langley Research Center
under Cooperative Agreement NCC1-01017

February 2005

Available from:

NASA Center for AeroSpace Information (CASI)
7121 Standard Drive
Hanover, MD 21076-1320
(301) 621-0390

National Technical Information Service (NTIS)
5285 Port Royal Road
Springfield, VA 22161-2171
(703) 605-6000

ABSTRACT

In conjunction with the research in ultra-lightweight deployable spacecraft and membrane structures is an underlying need for shape and vibration control. For thin film membrane structures, fundamental modes of vibration for the membrane can be excited through station keeping, attitude adjustments, orbital maneuvers, or contact with space junk or micrometeorites. In order to maintain structural integrity as well as surface shape contour, which may be essential for inflatable antennas, reflective surfaces, or solar sails; vibration damping is a necessary component. This paper discusses development of an actuator attached at the membrane boundary, containing two types of piezoelectric elements, which can be used to perform active control of vibration from the boundary of a membrane. The actuator is designed to control the membrane out-of-plane displacement and in-plane tension by varying the boundary conditions. Results from an initial experimental evaluation of the concept are presented with bench tests of the actuator alone, and with the actuator connected to a large membrane.

ACKNOWLEDGMENTS

The author wishes to acknowledge the people of The George Washington University JIAFS program, and the Structural Dynamics Branch at NASA Langley Research Center, for assistance enabling the completion of this research. Thanks to the academic advisor Dr. Paul A. Cooper, and Dr. Lucas Horta for continual help with analysis, technical advice, and support throughout the span of the research project. The author would also like to express gratitude to Andrew Panetta for help in design and modifications to the actuator and test setup, as well as Craig Savchenko, R. Wayne Mathews, David Kessler and Hoa Luong for technical assistance in experimental setup, and Dr. Olawale Adetona for assistance in testing with the membrane. Additional thanks go to Mercedes Reeves, and Dr. Eric Mockensturm for added analysis assistance and the computer gurus Gabrielle Snyder and Christopher Batten for their never-ending computer support. Thanks also go to Dr. Joe Blandino who helped to reaffirm the postulate that $NASA = GoodTimes \cdot e^{Fun^2}$ otherwise known as the Solter equation. Of course, the greatest gratitude of all goes to family, without whom none of this would have come about.

TABLE OF CONTENTS

LIST OF FIGURES

Number Page

LIST OF SYMBOLS AND ABREVIATIONS

Constants Definition

M_a - Mass of actuator

M_m - Mass of membrane

K_a - Spring coefficient of piezo bimorph

K_i - In-plane stiffness equivalent of membrane

K_o - Out-of-plane stiffness equivalent of membrane

L_c - Length of cable between actuator and membrane

α - The angle between the membrane c.m. and actuator c.m.

θ - Actuator cable angle

R - Unstretched length of in-plane spring (equivalent to radius of membrane)

F_c - Tension in the cable

F_u - Component force (of F_c) in the $\vec{u}$ direction

F_v - Component force (of F_c) in the $\vec{v}$ direction

T_c - Tension in the cable (experimental measurement equivalent to F_c)

T_m - Tension in the membrane (experimental measurement equivalent to F_u)

δM - Deflection of the membrane

Abbreviations

FRF - Frequency Response Function

PZT - Plumbum (lead) Zirconate Titanate; ceramic material used for piezo actuators

MFC - Macro-Fiber Composite

DSP - Digital Signal Processing

Chapter 1

INTRODUCTION

One aspect in the continuing venture to explore outer space focuses on lightweight gossamer spacecraft [1,2], including ultra-lightweight inflatable structures, large aperture telescopes, communication antennas, solar power systems and solar sails. A major consideration in the continued development of these types of spacecraft is vibration from active components attached to the spacecraft or excitations from external sources, and the potentially negative effects this type of motion can present in the quality of data collected from communications antennas, and telescopes, or even in the structural integrity of the spacecraft itself. For large structures, fundamental modes of vibration can often have very low frequencies and large deflections associated with them, which can be potentially fatal for the spacecraft or the science mission.

The necessity for vibration damping in space structures has been apparent for many years, though with more rigid structures the task of reducing vibrations to an acceptable level is much easier due to smaller magnitude deflections and the ability to add passive dampers. With thin film membranes, the issue of damping is more difficult. Large deflections, low fundamental frequencies, and the relatively small mass of membranes compound to provide high modal densities. Motion control and active vibration damping for these types of systems is necessary in order to maintain structural integrity, allow for proper performance, and provide a flightworthy spacecraft. The use of piezoelectric actuators is motivated by a desire to develop effective control devices for use on thin-film membranes with minimal addition to overall spacecraft mass. Piezo actuators are capable of producing large force outputs relative to their individual mass, and have a large operational bandwidth making them ideal candidates for use on gossamer spacecraft.

Research is being conducted on vibration control of inflatable membrane structures by using piezo actuators. However, much of this research involves actuators on the membrane itself [3]. This research is conducted with piezo patch elements that are bonded directly onto the membrane, providing excitation from within the membrane structure. The piezoelectric actuators generally have a much higher stiffness coefficient than the membrane materials, making them incompatible with the membrane materials and producing difficulties in modeling. Modal testing has, however, shown that this type of excitation produces very good agreement with other forms of excitation such as linear shakers, on the same article. It has been shown that positive position feedback (PPF) control provides significant reduction in vibration levels [4].

Other research is being conducted on vibration and shape control by using a membrane comprised of active piezo material [5]. This method utilizes a piezoelectric bimorph membrane material, which is excited using an electron gun to change the local shape of the material. The electron gun scans the membrane and applies increased or decreased electron energy to remove or build up excess electrons respectively. The shape of the membrane can be maintained accurately and adjusted to account for deformations. Much of this work focuses on control of the membrane on the interior of the actual article itself rather than on control of the membrane from the boundary.

A different approach to membrane control is the application of actuators at the boundary. This type of control varies the boundary conditions for the system, effectively changing the dynamics without adding mass directly to the membrane or directly manipulating the membrane itself. The ability to control membrane vibrations from the boundary has not yet been established. This thesis will focus on the design and fabrication of an actuator for boundary application to a membrane and the resulting ability of the actuator to provide dynamic damping to an excited membrane.

Chapter 2

SYSTEM DESCRIPTION

Prototype Membrane Actuator

The actuator described in this paper is designed to provide out-of-plane displacement excitation as well as in-plane tension force adjustment, while weighing only 6.2 oz (176.04 g). The actuator consists of an aluminum housing structure, two types of piezo actuators, and a cable, which is used to connect the actuator to the membrane. A piezo-stack is placed in-line with a cable connected to the membrane to provide in-plane tension adjustment. In addition, a bimorph piezo actuator bonded to a thin leaf spring supports the piezo stack housing and cable arrangement. Figure 2.1 shows a diagram of the actuator and the operation of the stack and its effect on the in-plane motion of the membrane as well as the operation of the piezo bimorph to produce out-of-plane motion. In-plane motion is produced through an extension or compression of the stack, effectively pulling the apex of the cable closer to the housing or allowing it to move farther out respectively. Out-of-plane motion is produced through bending of the cantilevered piezo bimorph, allowing the housing mass to deflect out-of-plane.

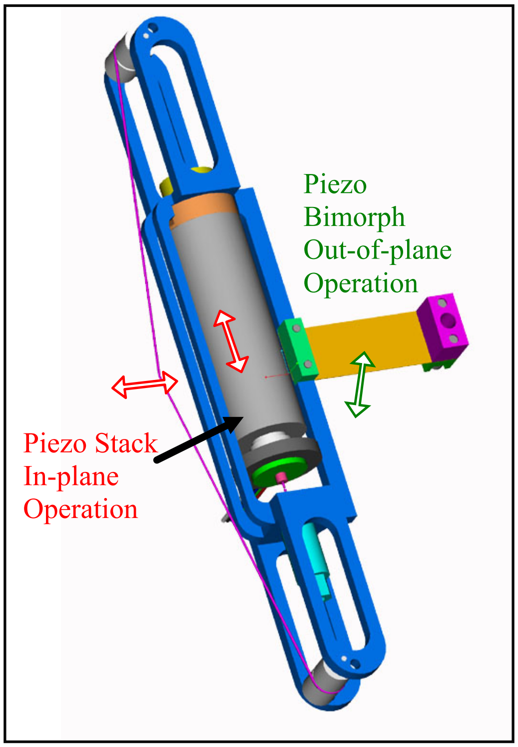

Figure 2.1 Actuator operation diagram

Two test setups were used for actuator performance evaluation, a bench test setup of the actuator alone and a setup with the actuator installed on the membrane (insitu). Figure 2.2 shows the actuator insitu with the membrane. Actuator performance data collected shows performance capabilities of both the piezo stack element and bimorph element under varying operational load conditions.

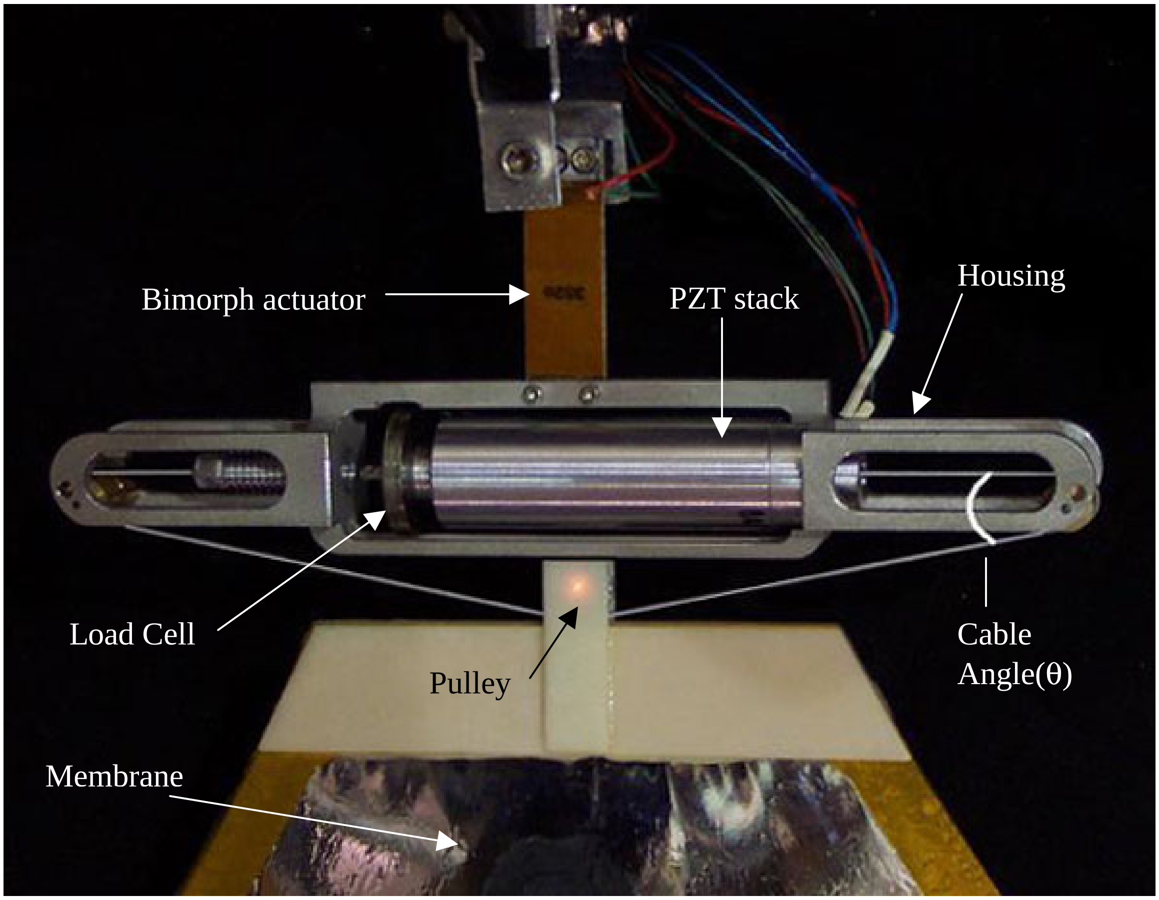

Figure 2.2 Operational configuration of actuator attached a membrane

The actuator is placed in the load path of the membrane to act as a filter, by stopping or reducing the transmission of structural vibrations from the hexapod structure to the membrane. During spacecraft operation, disturbances are introduced in the membrane through the support structure from station keeping maneuvers, orbital changes, or attitude adjustments. It is these sources of excitation that the actuator is intended to control.

Due to problems with creep seen in a Kevlar® cable, a 0.037 in (0.939 mm) diameter, nylon covered, braided steel cable was selected for testing and experimentation. The cable wraps around oil impregnated brass (oilite) sleeves 0.375 in (9.525 mm) in diameter, on either side of the actuator housing. The oilite sleeves rotate around a hardened steel dowel.

The actuator uses two types of piezo actuators to deliver in and out-of-plane excitation. The bimorph type piezo actuator shown in figure 2.3 is a 0.005 in (0.127 mm) thick Macro Fiber Composite (MFC-2) patch developed at NASA Langley Research Center [6,7]. The piezo bimorph measures 0.625 in (15.875 mm) wide by 1.5 in (38.1 mm) long. Two of these MFC-2 actuators are attached to each side of a 0.013 in (0.33 mm) thick metal leaf spring for out-of-plane actuation. An applied voltage creates a piezoelectric strain, producing a bending effect in the leaf spring. This bending effect produces the out-of-plane displacement of the housing, and as a result, the out-of-plane motion of the membrane at the attachment point.

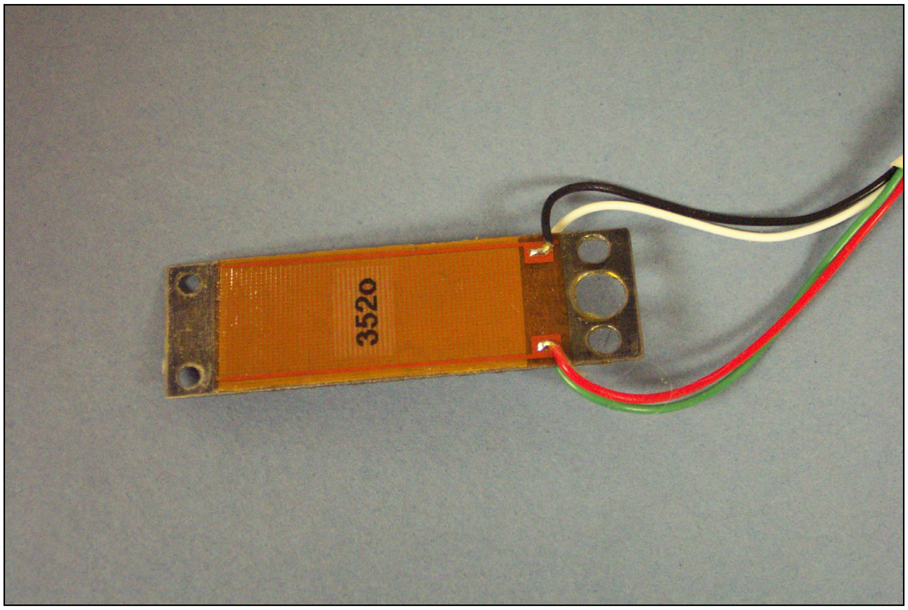

Figure 2.3 Piezo bimorph actuator

The piezo bimorph can be excited using only one of the piezo elements, with the second element acting as a dynamic strain sensor. This configuration diminishes the capability of the actuator to deliver out-of-plane motion, but provides a feedback sensor, which can be used for control.

The second type of piezo element is a Piezomechanik PZT ceramic ring type piezo stack encased in an aluminum housing as shown in figure 2.4. Expansion and contraction of the piezoelectric element, due to applied voltages, causes a lengthening or shortening of the stack. The actuator is used to increase and decrease the effective length of a tensioned cable passing through the center ring of the element, ultimately changing the membrane tension.

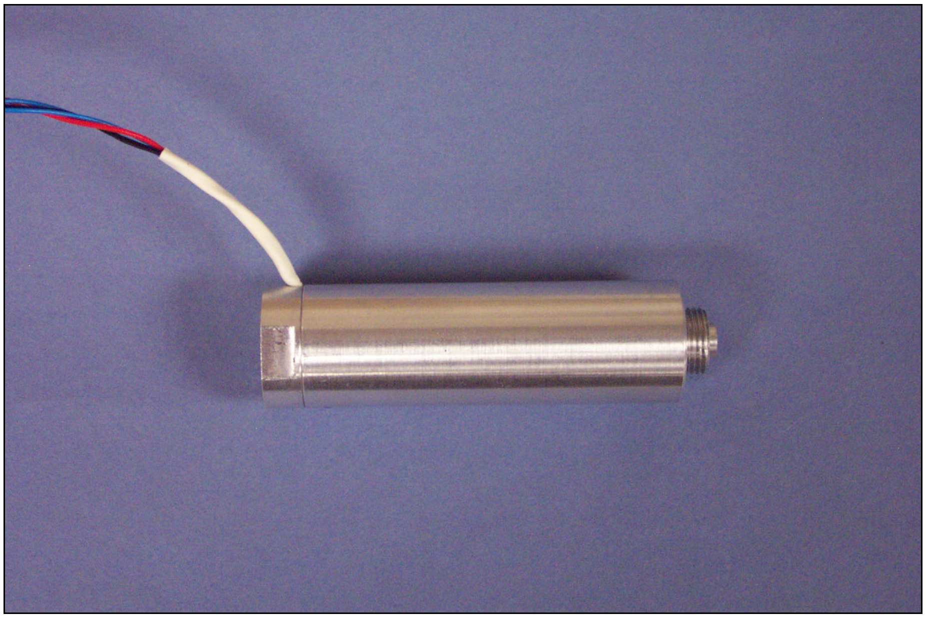

Figure 2.4 PZT stack actuator

The stack is capable of withstanding high compressive loads up to 1,348 lbs (6000 N), which is optimal for the proposed configuration. A compressive preload of 10% of the maximum load is applied to the stack, and, for this configuration, the additional compressive load applied by the actuator can be up to 80 lbs (355 N). This actuator is used for high precision, low displacement applications. Because the actuator is bipolar, it allows for expansion and some contraction (+150 V to – 30 V). The maximum stroke is approximately 2.52×10^{-3} in (64 μm) which should produce a maximum in-plane deflection at the apex of the cable of approximately 0.0073 in (185.3 μm) when the cable is at an angle of 10˚.

Membrane and Hexapod

The test article for which this research was conducted consists of three main components: a fiber composite hexapod support structure, a circular reflective membrane, and displacement actuators, 12 of which will provide boundary control of the membrane. The membrane and hexapod structure were manufactured by ILC Dover Inc. and the actuators were designed and manufactured at NASA Langley Research Center. Three actuators have been manufactured and are being tested to verify their capability to provide sufficient control authority and to verify robustness of the design before proceeding to build a final set.

Figure 2.5 shows the hexapod structure, with a flat reflective membrane stretched within a segmented torus structure, manufactured by ILC Dover Inc. The hexapod stands approximately 12 feet (3.66 m) as shown in figure 2.5. The hexapod structure is fabricated from 2 ply fiber carbon epoxy composite material 0.007 in (0.178 mm) thick. The membrane is held in tension within a dodecahedron torus, each leg of which is a circular composite tube 7.130 in (18.11 cm) in cross sectional diameter. The twelve segments of the torus structure are connected with polyurethane coupling joints. The torus is connected to an aluminum triangle primary using six tapered composite tubes, 104 in (2.644 m) from the front side of the torus. The three leg pairs extending from the back side of the torus are conical composite tubes with a small end outside diameter of 3.130 in (79.5 mm), and a large end outside diameter of 5.130 in (130 mm).

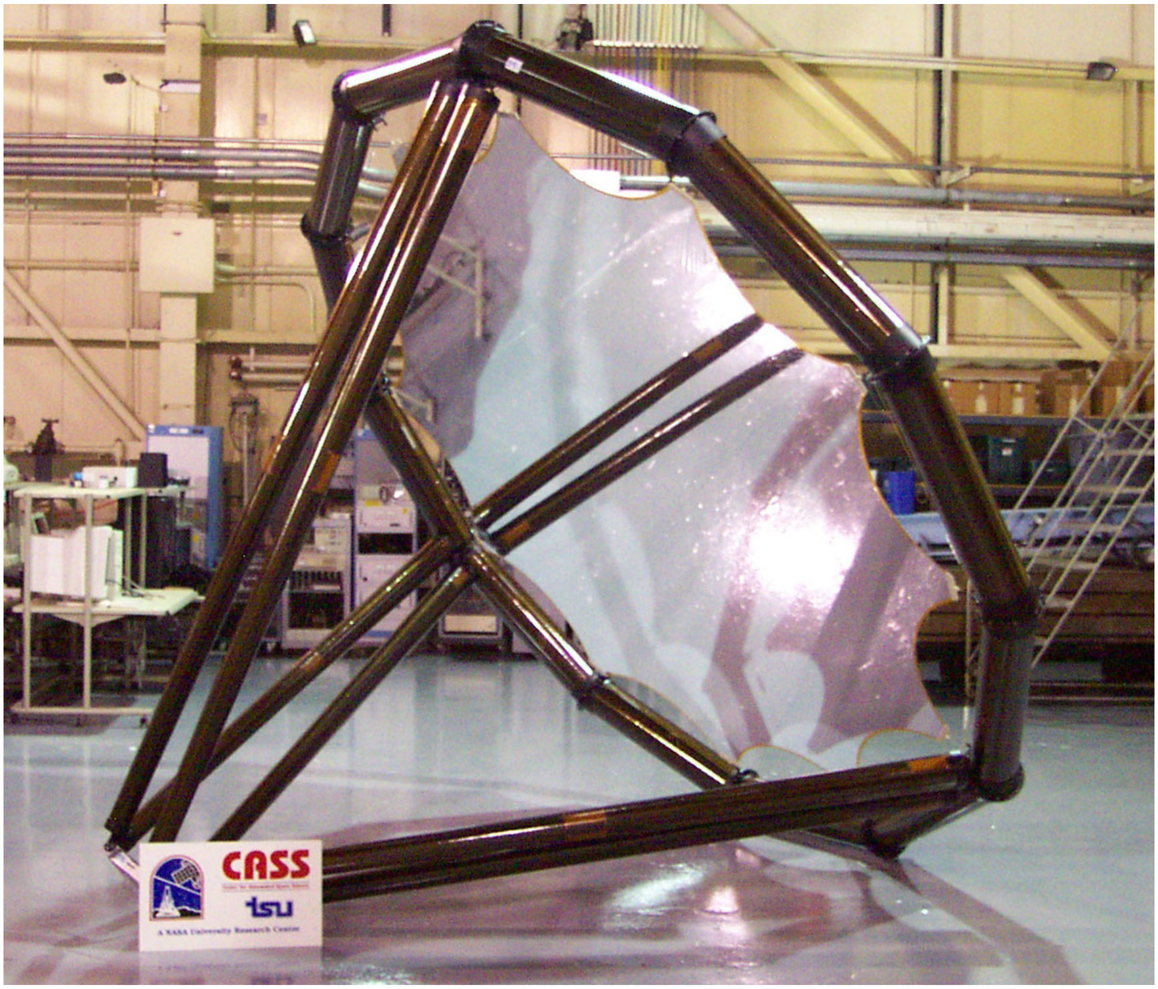

Figure 2.5 Hexapod structure and reflective membrane

The membrane is a circular membrane with a diameter of 105 in (2.667 m). There are twelve catenaries to provide tension distribution around the circular membrane, and also help to minimize membrane wrinkling. Figure 2.5 shows the membrane with the initial designed tension at each pull point of approximately 16 lbs (66.72 N). The membrane material is a vapor deposited, aluminum coated 0.001 in (25.4 μm) Kapton®. The legs of the hexapod structure can be seen across the membrane, which shows the reflective quality of the membrane surface. Due to the large size of the membrane, it must be assembled from multiple strips of material, which are joined together with adhesive seams.

Chapter 3

ANALYTICAL MODELING

Dynamics: A Simplified Approach

Due to the complex nature of the problem and the nonlinear behavior of the membrane, mathematical modeling for this type of problem is somewhat challenging. In order to better understand the problem, the actuator and membrane system are modeled using a simplified 2-D analytical dynamics model.

A lumped-mass representation is used to model the actuator at the end of a thin beam element, with a cable connecting the actuator lumped mass to another lumped mass representing the membrane (figure 3.1). In order for this analysis to mimic the actual test article, the cable allows only tensile forces to be transmitted. The actuator model parameters are the bending stiffness of the piezo bimorph K_a, actuator mass M_a, membrane mass M_m, the distance between the actuator and the connection point on the membrane L_c, and the cable angle between the two lumped masses α. A simplified model of the membrane is used with an equivalent in-plane spring stiffness K_i, which has an un-stretched length R, and an out-of-plane equivalent spring stiffness K_o.

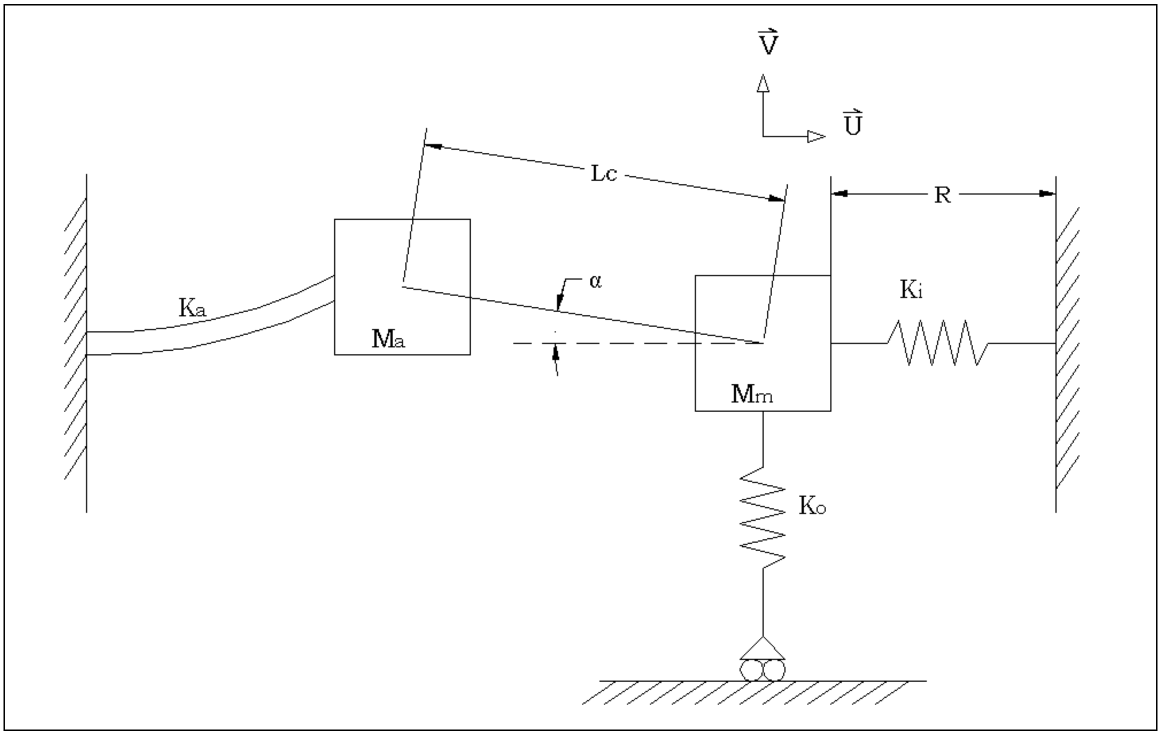

Figure 3.1 Simplified model of actuator and membrane for dynamics analysis

Figure 3.2 shows exaggerated positions of the deflected lumped masses. The in-plane spring provides two components of restoring force: in-plane ($\vec{u}$) and out-of-plane ($\vec{v}$), where $\vec{u}$ and $\vec{v}$ are unit orthogonal basis vectors. The magnitude of the computed out-of-plane stiffness for the membrane is two orders of magnitude less than the in-plane stiffness. Therefore the out-of-plane spring is allowed to roll with the membrane lumped mass, resulting in no restoring force in the rolling direction.

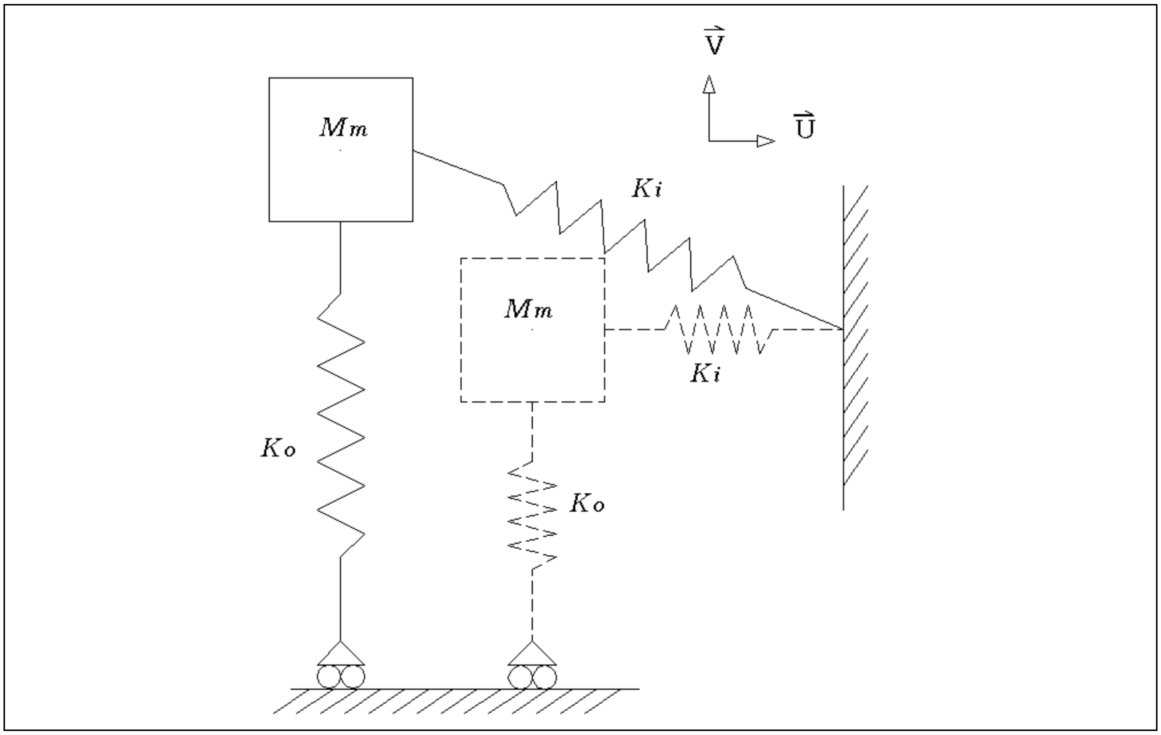

Figure 3.2 Membrane deflection position

Using vector analysis and an assumed displacement of the membrane, the force can be calculated in each of the springs. Considering the membrane side of the mechanism, the force in the springs will result from a tension force, or out-of-plane excitation from the actuator. Figure 3.3 shows a vector representation of the displacement of the center of mass of the membrane. Consider point O in the undeformed position of the membrane c.m. to undergo a displacement to point D after being displaced by the actuator. The magnitude of the displacement in the $\vec{v}$ direction is V_m, and U_m in the $\vec{u}$ direction. Let δT be the total displacement of the membrane c.m. and S be the length of the stretched spring with stiffness K_i.

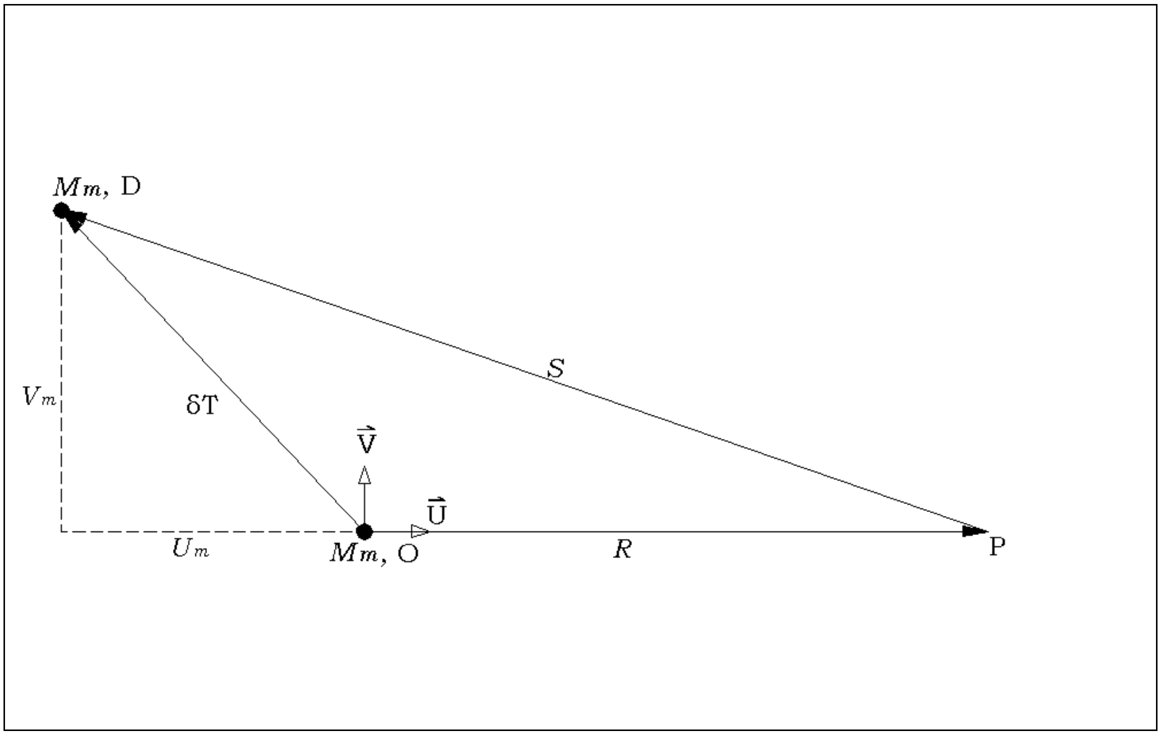

Figure 3.3 Assumed vector displacements of membrane

Using these definitions, a vector $\vec{S}$ can be written as

$$\vec{S} = -(Um + R)\,\vec{\mathbf{u}} + Vm\,\vec{\mathbf{v}} \tag{3.1}$$

to locate the mass M_m with respect to point P. The magnitude of the displacement is

$$\left\|\vec{S}\right\| = \sqrt{(Um + R)^2 + (Vm)^2} \tag{3.2}$$

To normalize the displacement vector in Eq. 3.1, divide Eq. 3.1 by Eq. 3.2 to get a unit vector $\hat{S}$ such that

$$\hat{S} = \frac{-(Um + R)\,\vec{\mathbf{u}} + Vm\,\vec{\mathbf{v}}}{\sqrt{(Um + R)^2 + (Vm)^2}} \tag{3.3}$$

The actuator pull force F_c (figure 3.4) represents the tension pull from the actuator to the membrane. Reaction forces F_{Ki} and F_{Ko} are the forces on the in and out-of-plane springs, respectively. Force from the in-plane spring can be broken into $\vec{u}$ and $\vec{v}$ components.

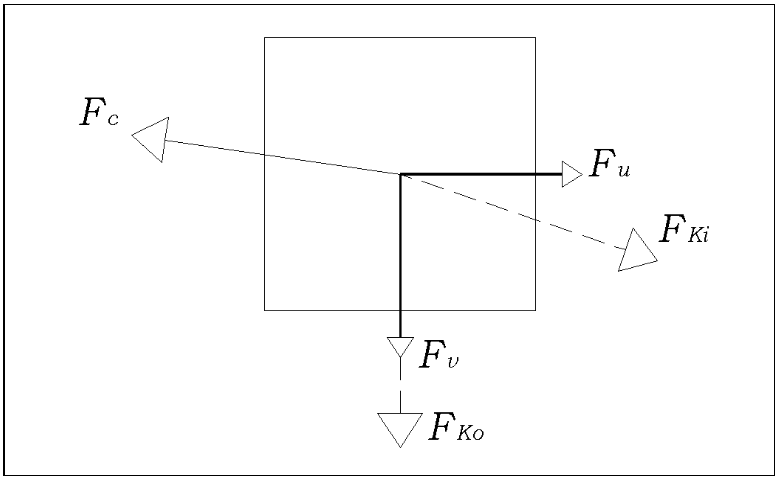

Figure 3.4 Spring reaction forces on the membrane

The force from the in-plane spring can be written as

$$F_{Ki} = -K_i \cdot \left(\left\|\vec{S}\right\| - R\right) \cdot \hat{S} \qquad 3.4$$

and the force from the out-of-plane spring is

$$F_{Ko} = -K_o \cdot Vm\, \vec{\mathbf{v}} \qquad 3.5$$

The spring force equations can be further reduced to component force equations, which can further be reduced by using a Taylor series expansion. Due to the small values of U_m and V_m, the expansion is only carried out to third order elements.

The component force in the $\bar{u}$ direction is

$$F_u = \left[K_i U_m + K_i \cdot \frac{V_m{}^2}{2R} \right] \vec{\mathbf{u}} \tag{3.6}$$

The component force in the $\bar{v}$ direction is

$$F_v = \left[- K_o V_m - K_i \left(\frac{U_m V_m}{R} + \frac{V_m{}^3}{2R^2} \right) \right] \vec{\mathbf{v}} \tag{3.7}$$

From the component forces, the total change in tension pull force being applied to the membrane can be calculated. This force is used in the equations of motion for the membrane lumped mass, and also as an output to determine how much tension the membrane is subjected to and what change in tension the actuator is theoretically capable of. Using the force components, the cable force magnitude is

$$\left\| F_c \right\| = \sqrt{\left[K_i \left(U_m + \frac{V_m{}^3}{2R} \right) \right]^2 + \left[- K_o V_m - K_i \left(\frac{U_m V_m}{R} + \frac{V_m{}^3}{2R^2} \right) \right]^2} \tag{3.8}$$

Considering the cable mechanism, the system is constrained by the length of the cable connecting the two lumped masses. A 2-D representation is used to model the distance between the axial center of the stack element of the actuator and the physical connection point of the membrane.

Figure 3.5 shows an exaggerated displacement condition of the two lumped masses and the connection geometry between them. *Va* represents the out-of-plane deflection of the actuator, while V_m represents the deflection of the membrane. $V_{a/m}$ is the difference between V_a and V_m in the $\vec{v}$ direction. Due to the nature of the bimorph bending to produce the out-of-plane displacement, the in-plane deflection of the actuator lumped mass is considered to be negligible compared to the out-of-plane deflection. In-plane actuation comes from the change in length of L_c and is not considered to affect the actuator mass. The changed length from the original nominal distance L_c is represented as L'_c. The in-plane deflection of the membrane is U_m, and $U_{a/m}$ is the distance in the $\vec{u}$ direction between U_a and U_m. From the constraint geometry, a constraint equation can be obtained and the system equations of motion can be completed.

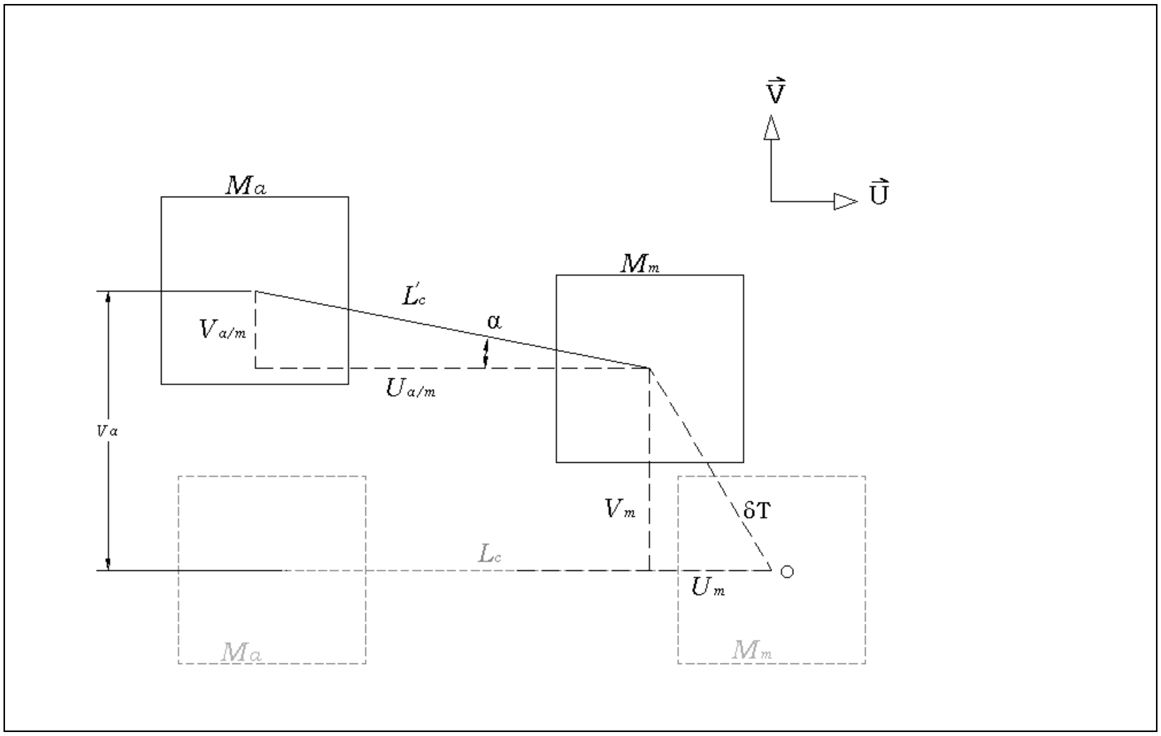

Figure 3.5 Constraint geometry for the displaced masses

The constraint equation for the length L'_c is

$$L'_c = \sqrt{(L_c - U_m)^2 + (V_a - V_m)^2} \tag{3.9}$$

and the angle relations for α can be written as

$$\sin\alpha = \frac{V_a - V_m}{L'_c} \qquad 3.10$$

and,

$$\cos\alpha = \frac{L_c - U_m}{L'_c} \qquad 3.11$$

Due to the nonlinear nature of the in-plane spring acting in the out-of-plane direction, the equations of motion contain both linear and non-linear components. The equation of motion for the mass representing the membrane in the in-plane direction:

$$M_m\ddot{U}_m + K_i U_m + K_i\left(\frac{V_m{}^2}{2R}\right) = F_c\cos\alpha = F_c\left(\frac{L_c - U_m}{L'_c}\right) \qquad 3.12$$

and the equation of motion for the mass representing the membrane in the out-of-plane direction is

$$M_m\ddot{V}_m + K_o V_m + K_i\left(\frac{U_m V_m}{R} + \frac{V_m{}^3}{2R^2}\right) = F_c\sin\alpha = F_c\left(\frac{V_a - V_m}{L'_c}\right) \qquad 3.13$$

If one defines the state vector $\begin{Bmatrix} X_1 \\ X_2 \\ Y_1 \\ Y_2 \end{Bmatrix}$ where $X_1 = U_m \quad X_2 = \dot{U}_m \quad Y_1 = V_m \quad Y_2 = \dot{V}_m$

The equations of motion can be represented as four 1st order nonlinear ordinary differential equations, which in matrix form are

$$\begin{Bmatrix}\dot{X}_1\\ \dot{X}_2\\ \dot{Y}_1\\ \dot{Y}_2\end{Bmatrix} = \underbrace{\begin{bmatrix}0 & 1 & 0 & 0\\ -\dfrac{K_i}{M_m} & 0 & 0 & 0\\ 0 & 0 & 0 & 1\\ 0 & 0 & -\dfrac{K_o}{M_m} & 0\end{bmatrix}}_{Linear}\begin{Bmatrix}X_1\\ X_2\\ Y_1\\ Y_2\end{Bmatrix} + \underbrace{\begin{bmatrix}0\\ -K_i\left(\dfrac{Y_1^{\,2}}{2R}\right)+F_c\left(\dfrac{X_1}{L_c'}\right)\\ 0\\ -K_i\left(\dfrac{X_1Y_1}{R}+\dfrac{Y_1^{\,3}}{2R^2}\right)+F_c\left(\dfrac{V_a-X_1}{L_c'}\right)\end{bmatrix}}_{non\text{–}linear} \qquad 3.14$$

The beam element supporting the actuator mass M_a is modeled using a finite element solution, which incorporates the bending stiffness K_a, and the voltage to strain relation for the piezo bimorph actuator. The finite element model, created using NASTRAN®, is used to model the metal leaf spring with the bimorph actuator bonded to both sides. The 80-element NASTRAN model provides dynamic characteristics of the bimorph and leaf spring, and a rigid finite element on the end of the leaf spring represents the actuator housing. Appropriate mass characteristics are included for the elements representing the actuator housing.

A diagram of the NASTRAN model is shown in figure 3.6, with grid points 78,79, and 80 on a rigid element representing the actuator housing. The unit vector $\vec{w}$ shown is in the tangential in-plane direction and is not utilized in the 2-dimensional analysis. Cable forces are applied at grid points 79 and 80 with no resultant force in the $\vec{w}$ direction. Outputs from the finite element model include deflections, and accelerations of points 78, 79, and 80 in the $\vec{u}$, $\vec{v}$, and $\vec{w}$ directions.

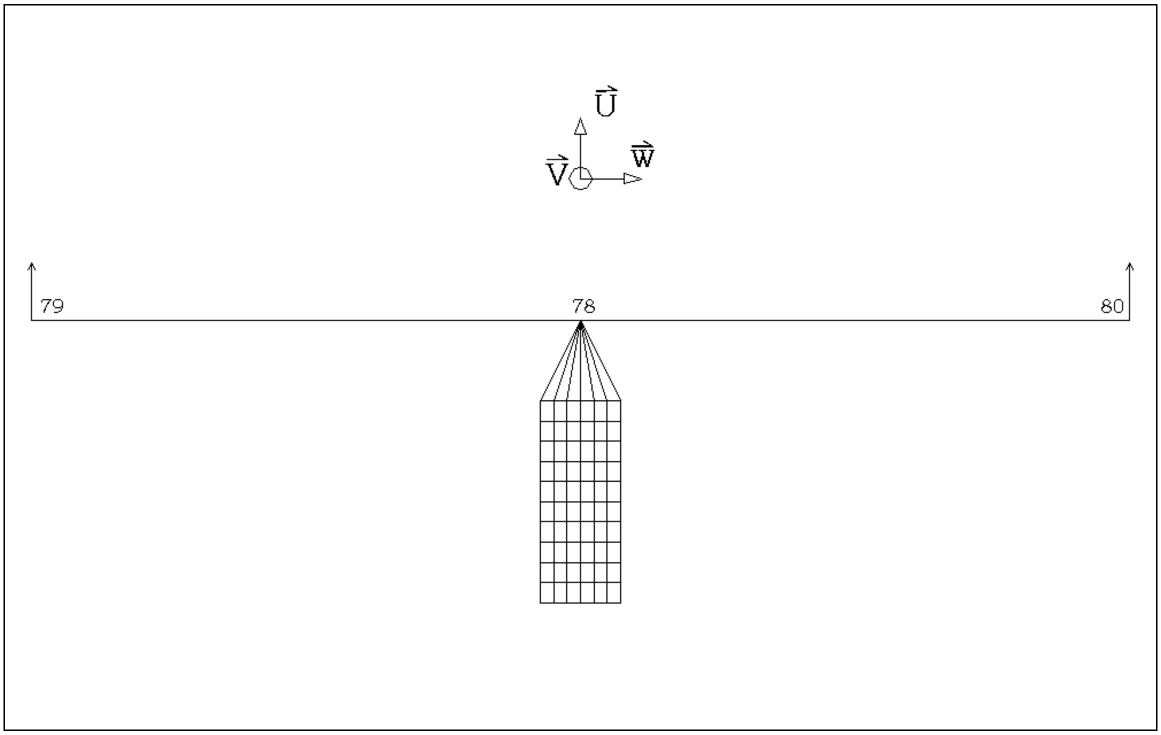

Figure 3.6 NASTRAN model of actuator

The model is converted from a finite element model to a state space representation of the system [**8**], shown in figure 3.7.

The state space model has 5 inputs, and 18 outputs. The inputs include voltage to the piezo bimorph and forces on the rigid element in the in-plane and out-of-plane directions for the two outer nodes of the actuator housing (elements 79 and 80).

$$\begin{bmatrix} \underbrace{\begin{bmatrix} A \end{bmatrix}}_{20\ \text{x}\ 20} & \underbrace{\begin{bmatrix} B \end{bmatrix}}_{20\ \text{x}\ 5} \\ \underbrace{\begin{bmatrix} C \end{bmatrix}}_{18\ \text{x}\ 20} & \underbrace{\begin{bmatrix} D \end{bmatrix}}_{18\ \text{x}\ 5} \end{bmatrix}$$

Figure 3.7 State space representation of bimorph

The FEA model, the previously described equations of motion, and the constraint equation combine to form a complete set of equations that model the dynamic behavior of the entire mechanism.

Cable Geometric Analysis

In-plane tension adjustments are accomplished using an extensible piezo stack actuating a cable wrapped around two pulleys (figure 3.8). In this arrangement, the cable angle is an important factor in the performance of the piezo stack. Cable angle is a function of the initial pretension level, with high initial pretension levels producing small initial cable angles at the same membrane tension. Tension in the actuator cable (T_c) is related to the membrane tension (T_m), and the angle θ as follows:

$$2T_c \sin\theta = T_m \qquad 3.15$$

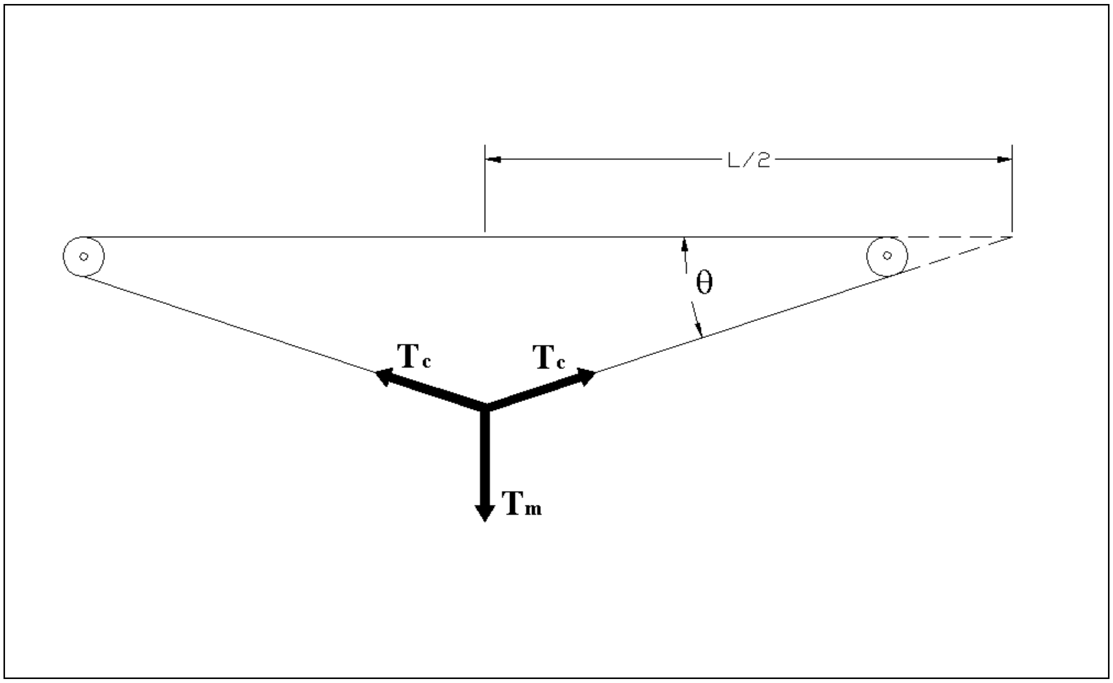

Figure 3.8 Cable force geometry

The geometric length L/2 varies with the angle θ. Figure 3.9 shows the relationship between the cable angle θ and the length L/2 for cable angles ranging from 9º to 13º. Later calculations will use these L/2 values to compare calculated results with experimental data. The length L/2 varies by as much as 0.74 in (18.80 mm) based on the cable angle chosen.

θ (deg)	L/2 (in)
9	5.93
9.5	5.80
10	5.69
10.5	5.59
11	5.49
11.5	5.41
12	5.33
12.5	5.25
13	5.19

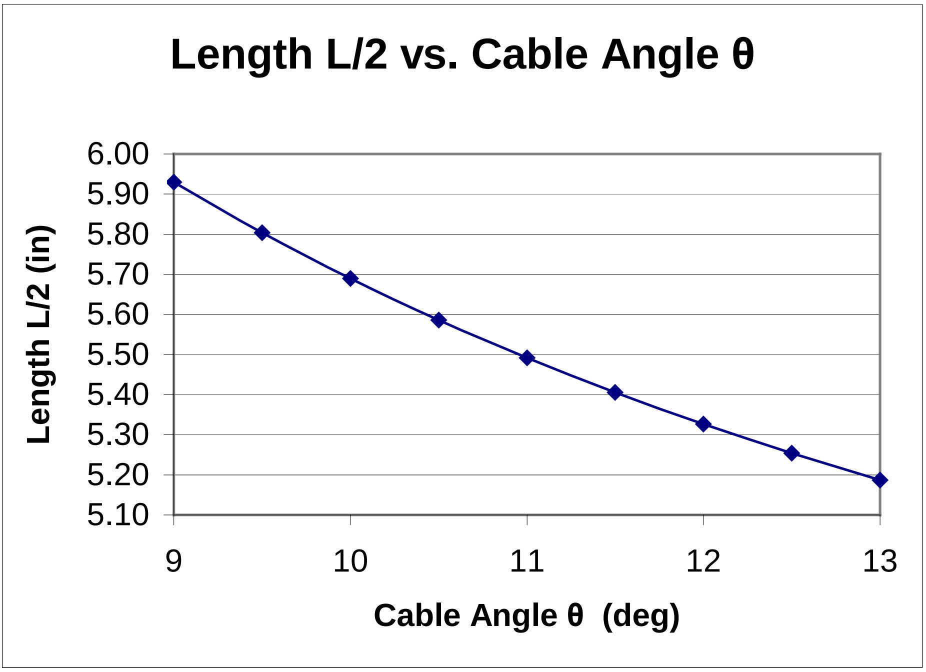

Figure 3.9 Length of L/2 as a function of cable angle ***θ***

The stack and cable configuration shown in figure 3.8 effectively amplifies the motion of the stack at the membrane attachment point. To evaluate the mechanical advantage of the cable actuator configuration, consider the geometry of the system shown in figure 3.10.

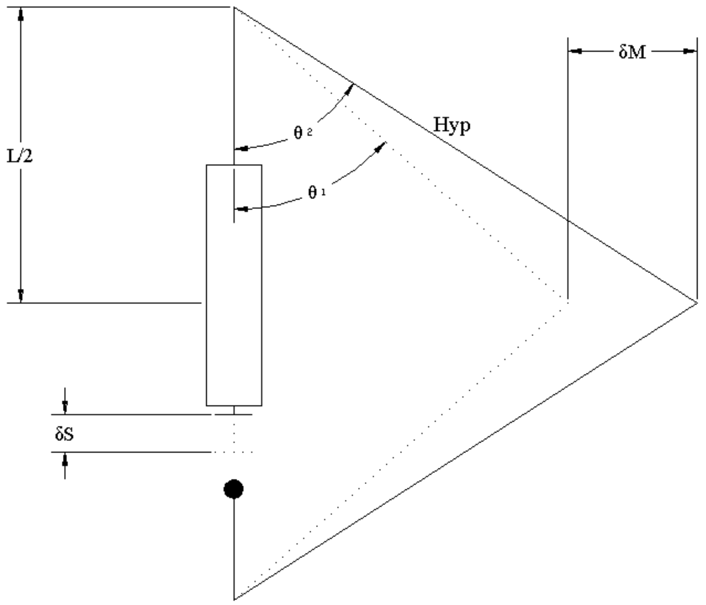

Variable	Description	Units
δM	In-plane membrane deflection	inches
δS	Stack deflection	inches
θ_1	Starting cable angle	degrees
θ_2	Ending cable angle (after deflection)	degrees
Hyp	Length of hypotenuse	inches
L/2	One half the length of the actuator housing	inches

Figure 3.10 Membrane displacement and stack displacement geometry (picture not to scale)

Using the geometry in figure 3.8 a relationship between actuator displacement δS, membrane displacement δM, and cable angle can be formulated. Knowing the initial cable angle, the hypotenuse length is

$$\text{Hyp} = \frac{L}{2\cos(\theta_1)} \qquad 3.16$$

Taking into account a displacement of the stack (δS), and the fact that the hypotenuse will be shorter by $\delta S/2$ to maintain equilibrium, the cable angle after displacement is

$$\theta_2 = \cos^{-1}\left(\frac{L}{2}\cdot\frac{1}{\mathrm{Hyp}-\frac{\delta S}{2}}\right) \qquad 3.17$$

Knowing these two variables, the in-plane displacement of the stack can be easily computed to be

$$\delta M = \frac{L}{2}\left(\tan(\theta_1)-\tan(\theta_2)\right) \qquad 3.18$$

Figure 3.11 shows the functional relation between in-plane membrane deflection and the deflection of the stack at different cable angles. It can be seen that at smaller cable angles there is a larger mechanical advantage, and the slope for that portion of the graph is considerably steeper. Note that the graph shows that the deflection of the stack is essentially unidirectional, despite the fact that there is some capability of the stack to contract by a small amount. The maximum deflection value of 2.52×10^{-3} in (64 μm) for the stack, as reported by the manufacturer, is used for this study.

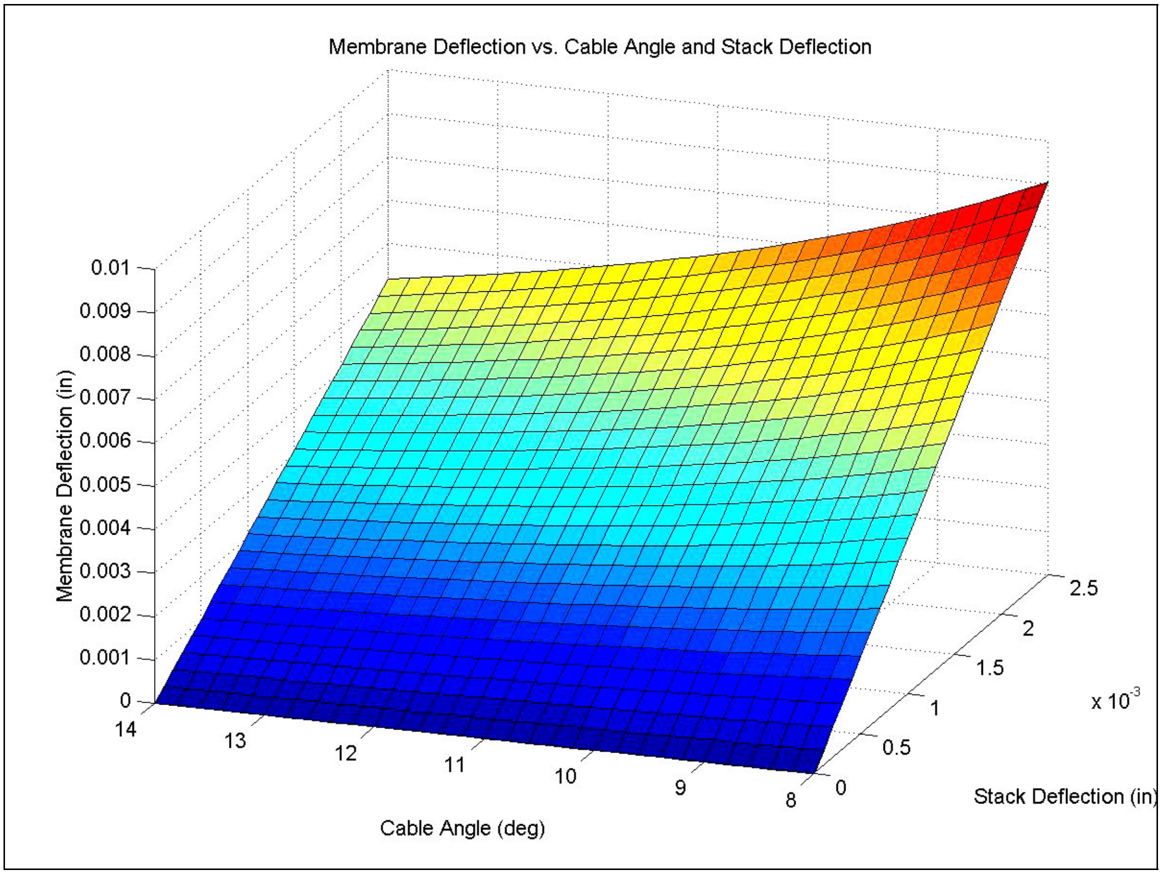

Figure 3.11 Membrane deflection vs. stack deflection for various cable angles

Chapter 4

DYNAMIC SIMULATION OF ACTUATOR AND MEMBRANE SYSTEM

Description

A dynamic simulation of the actuator and membrane using MATLAB® and Simulink® was created to assess the control authority of the actuator on the membrane under different loading conditions. Physical inputs to the system include voltage to the stack and voltage applied to the piezo bimorph. The simulation is designed to accept voltage signal inputs for both piezo actuators and to output the overall actuator dynamics, the displacements of the membrane center of mass, and the tension load in the cable.

The simulation incorporates a finite element model for the piezo bimorph with the bonded piezo-ceramic and the dynamic equations of motion for the cable actuation system shown in the previous chapter. In order to incorporate both models and solve the coupled system of equations, a MATLAB s-function is used. The s-function allows multiple variable parameters to be passed in to a single Simulink block that uses mathematical solution techniques to solve differential equations for continuous and/or discrete time systems. The solution for the non-linear state space equations and the constraint equation can be performed using the s-function equation solving capabilities. In order to solve the state space equations for the piezo bimorph, the forces on the actuator must be continuously updated and fed back into the system as an input. Figure 4.1 shows a diagram of the simulation scheme with inputs and outputs, and shows the force variables being fed back into the s-function.

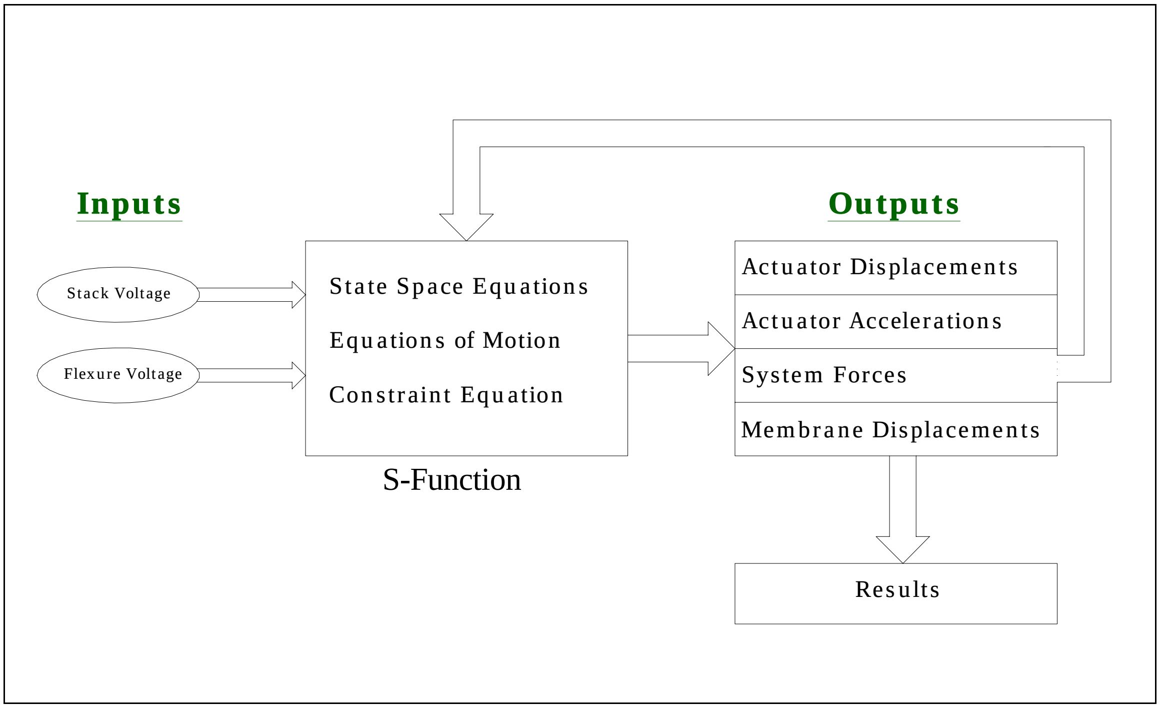

Figure 4.1 Simulation process flowchart

Analysis Results

To simulate the capability of the piezo stack, a staircase voltage with a maximum voltage of 150 V and a step size of 10 V, is applied to the stack input. Figure 4.2 shows the simulated profile of the stack actuation, with no voltage applied to the piezo bimorph. The graphs show the voltage profile to the piezo stack, the change in membrane tension, and the deflection of the membrane. Note that the values for membrane tension and deflection are changes in values, and not absolute load or displacement values. The computed maximum change in membrane tension is approximately 0.556 lbs (2.446 N). This value is a function of the expected maximum deflection of the piezo stack of 0.00252 in (64 μm), and the assumed cable angle of 10°. The membrane deflection is shown to be negative, which is a result of the coordinate convention assumed in the analysis that places the origin at the membrane pulley, and directs positive displacement toward the center of the membrane. The maximum in-plane deflection computed is 0.007 in (177.8 μm).

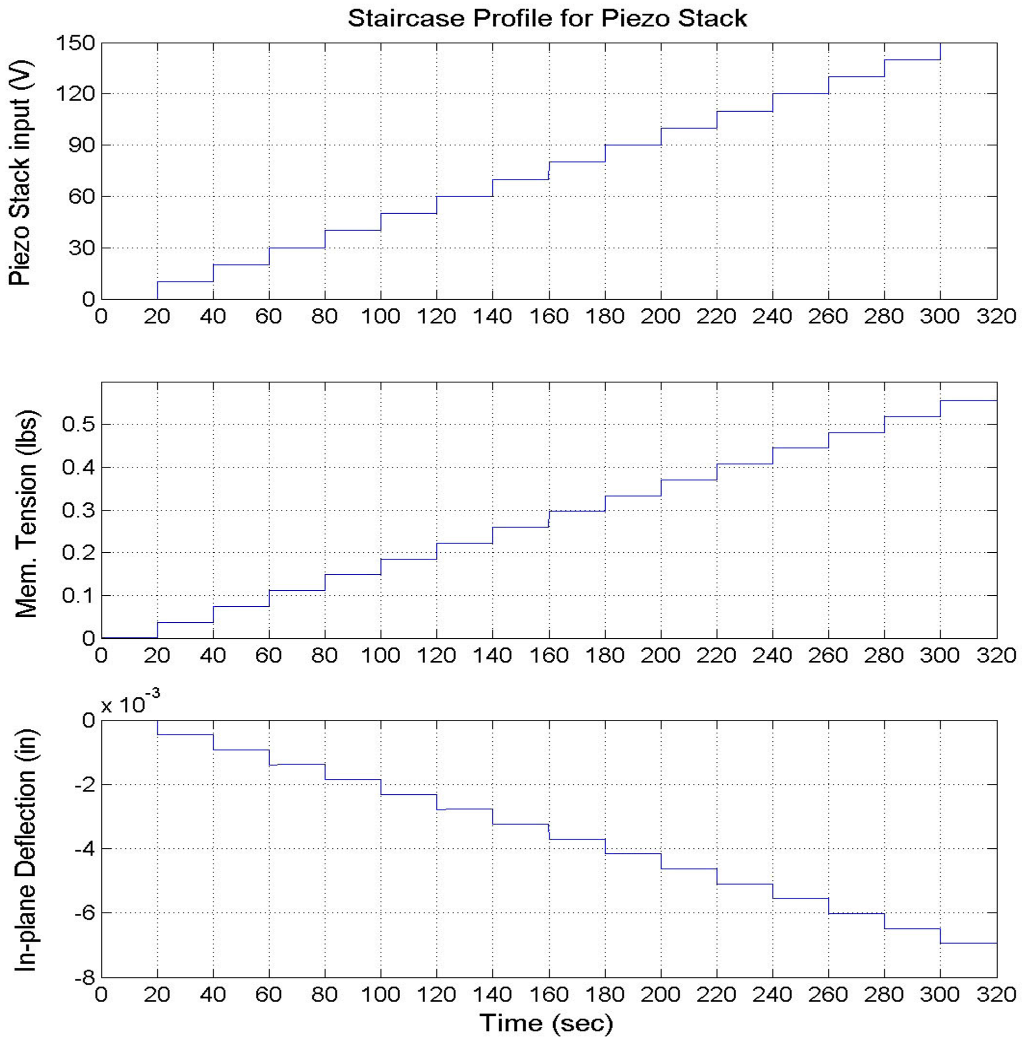

Figure 4.2 Simulation results for staircase voltage profile on piezo stack

Similar analysis is run on the piezo bimorph actuator, using a staircase profile with a maximum voltage of 450 V, and a step size of 30 V. Figure 4.3 shows results from top to bottom of the input voltage, change in membrane tension, out-of-plane deflection, and in-plane deflection of the membrane. In the graph, a natural oscillating effect can be seen in the membrane tension as well as in the deflection of the membrane. Damping was added to the system using an arbitrarily chosen damping value of 10%, to allow for the system to compute a steady state value for each step. The maximum change in membrane tension is approximately 0.193 lbs (0.858 N), with an out-of-plane deflection of 0.0042 in (106.7 μm). The in-plane deflection capability of the bimorph is approximately 0.0024 in (60.96 μm).

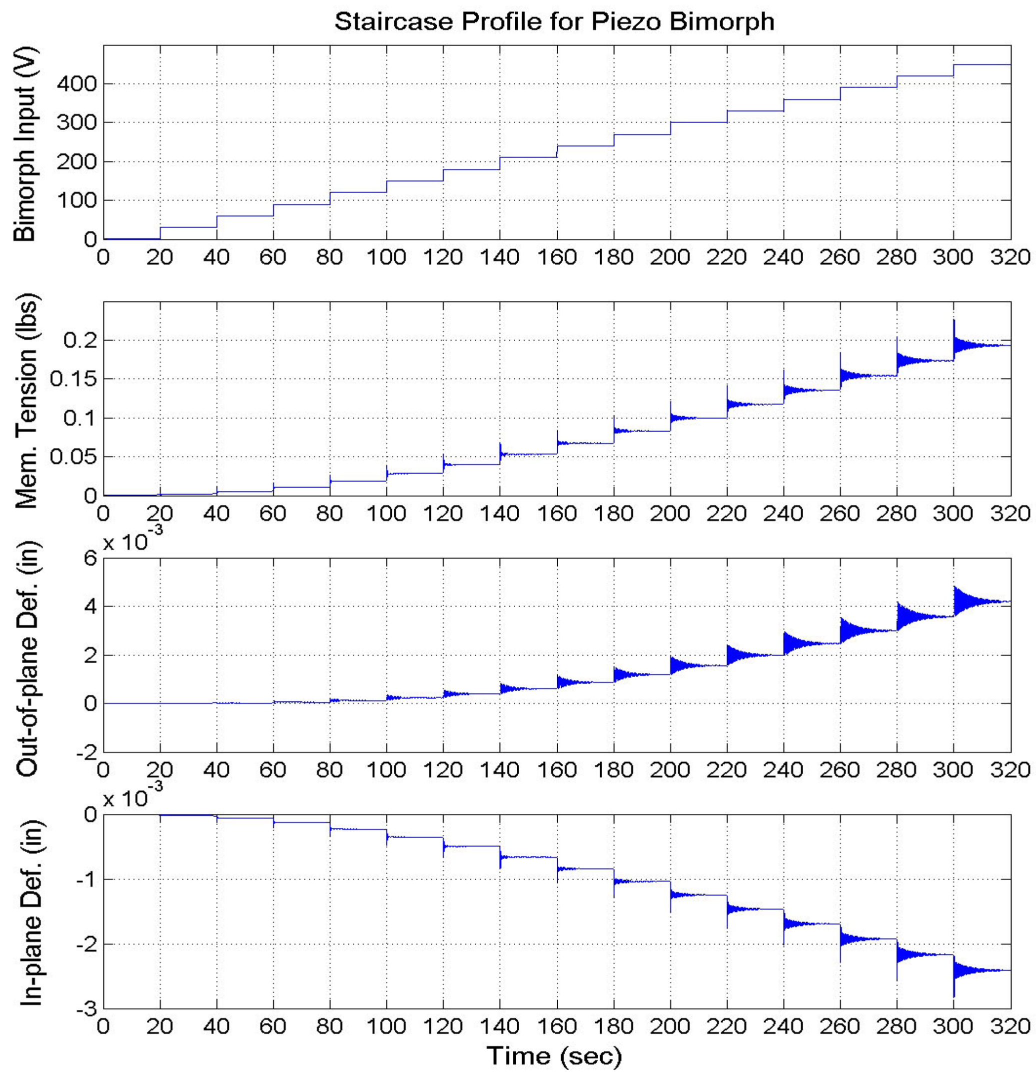

Figure 4.3 Simulation results for staircase voltage profile on piezo bimorph

An important feature to note from figure 4.3 is the non-linear nature of the deflection of the flexural actuator. These results show that only a small change occurs below 90 V, but between 250 V and 450V the performance is improved significantly. The in-plane deflection is very nearly linearly related to voltage.

Figure 4.4 shows results from the staircase voltage profiles commanded to both piezo actuators, the membrane tension, the out-of-plane deflection, and the in-plane deflection. Combining the staircase input signals for both piezo actuators simultaneously shows the maximum theoretical capability of the actuator. The maximum membrane tension adjustment with both piezo actuators is approximately 0.66 lbs (2.938 N). The maximum out-of-plane deflection using both actuators is 0.0105 in (266.7 μm) which is significantly higher than the result of 0.0042 in (106.7 μm) using only the bimorph actuator. The maximum in-plane deflection is approximately 0.0083 in (210.8 μm) which is a slight improvement over the piezo stack alone. As expected, the capability of the actuator is increased when both piezo actuators are utilized. The analytical results show the ability of the stack to dramatically improve the out-of-plane deflection capability of the flexural actuator.

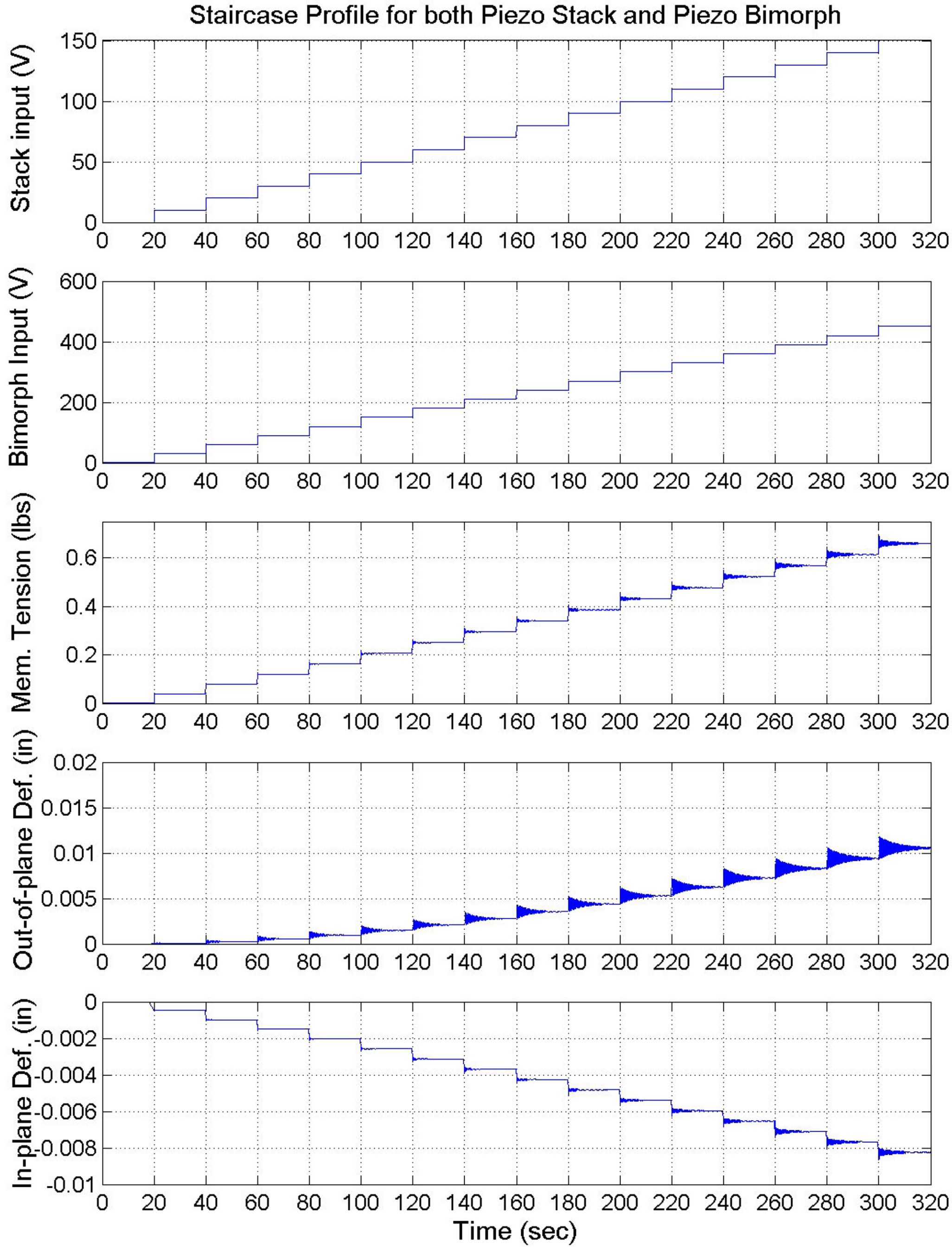

Figure 4.4 Simulation results for staircase voltage profile on stack and bimorph

For out-of-plane testing, the analytical model is linearized to compute a frequency response function (FRF). In order to accentuate the mode peaks, the damping for this simulation was set to 1%. This FRF can be used to compare results with the bench test and membrane test results. The FRF of the analytical model shows the first bending mode of the bimorph, and the migration of the resonant frequency with increasing load (figure 4.5). The FRF is taken with respect to point 78 (refer to figure 3.6). Note the second peak, at approximately 83 Hz, which changes very little and is apparently insensitive to tension load level. This is believed to be the second bending mode, though this apparent insensitivity to tension loading is unexplained.

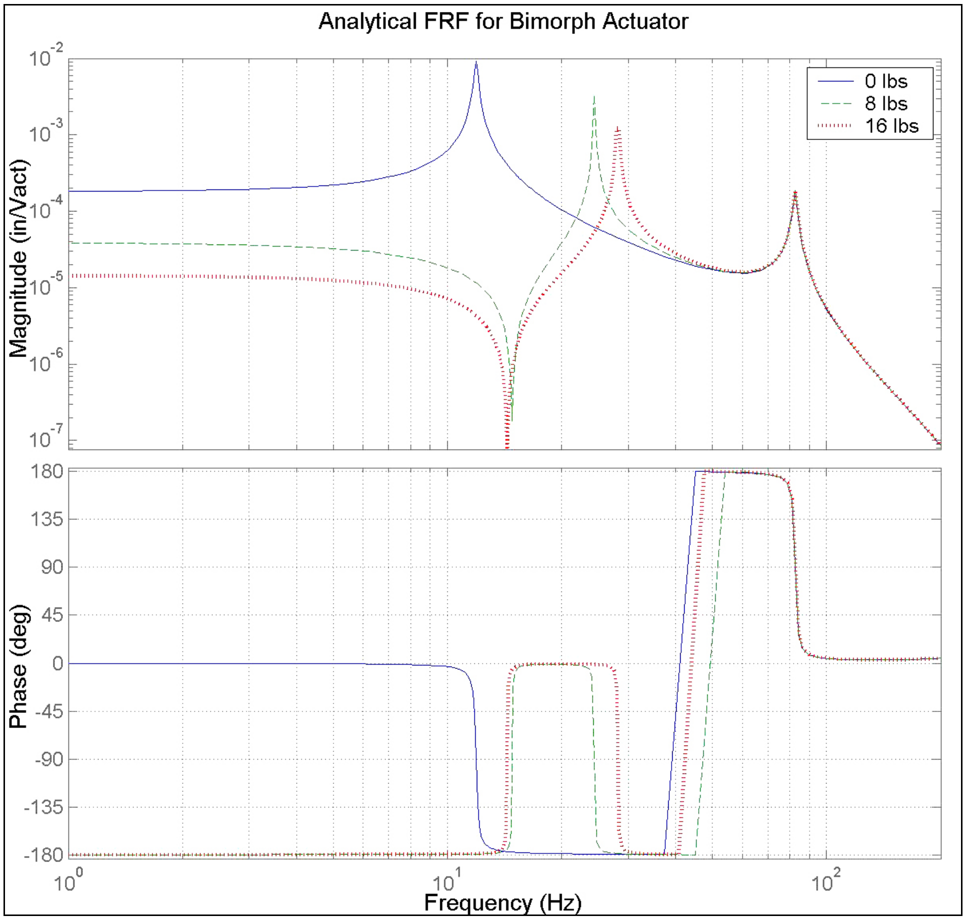

Figure 4.5 Frequency response of linearized model

Chapter 5

ACTUATOR BENCH TEST

Setup

In order to verify the capabilities of the actuator alone, a bench test, designed to allow for operation of the actuator under various loading configurations, is used. Figure 5.1 shows the bench test setup. A load cell is located at the membrane attachment point T_1, which provides data on the tension that would be applied to the membrane. A second load cell, located at T_2 at the end of the piezo stack, provides data on the tension in the cable. Measurement of in-plane displacement at the location T_1 is performed using a micrometer. A Keyence laser displacement sensor, not shown in the figure, is used to measure out-of-plane displacement of the flexural actuator.

An aluminum test fixture acts as a support structure for the actuator. The test fixture is a rectangular aluminum structure with a track running lengthwise to allow for positioning of the test article and measurement devices. The actuator is attached to a block at one end. At the opposite end a micrometer is held in position and allows for measurement of in-plane displacement with an accuracy of approximately 0.001 in (25.4 μm). The load cell at T_1 connects to the actuator cable through a round pulley to provide stress relief at the pull point. The test fixture is held in a vertical position to avoid any residual bending of the bimorph due to gravity loading. The stack load cell is located at one end of the stack actuator and measures the tension in the cable.

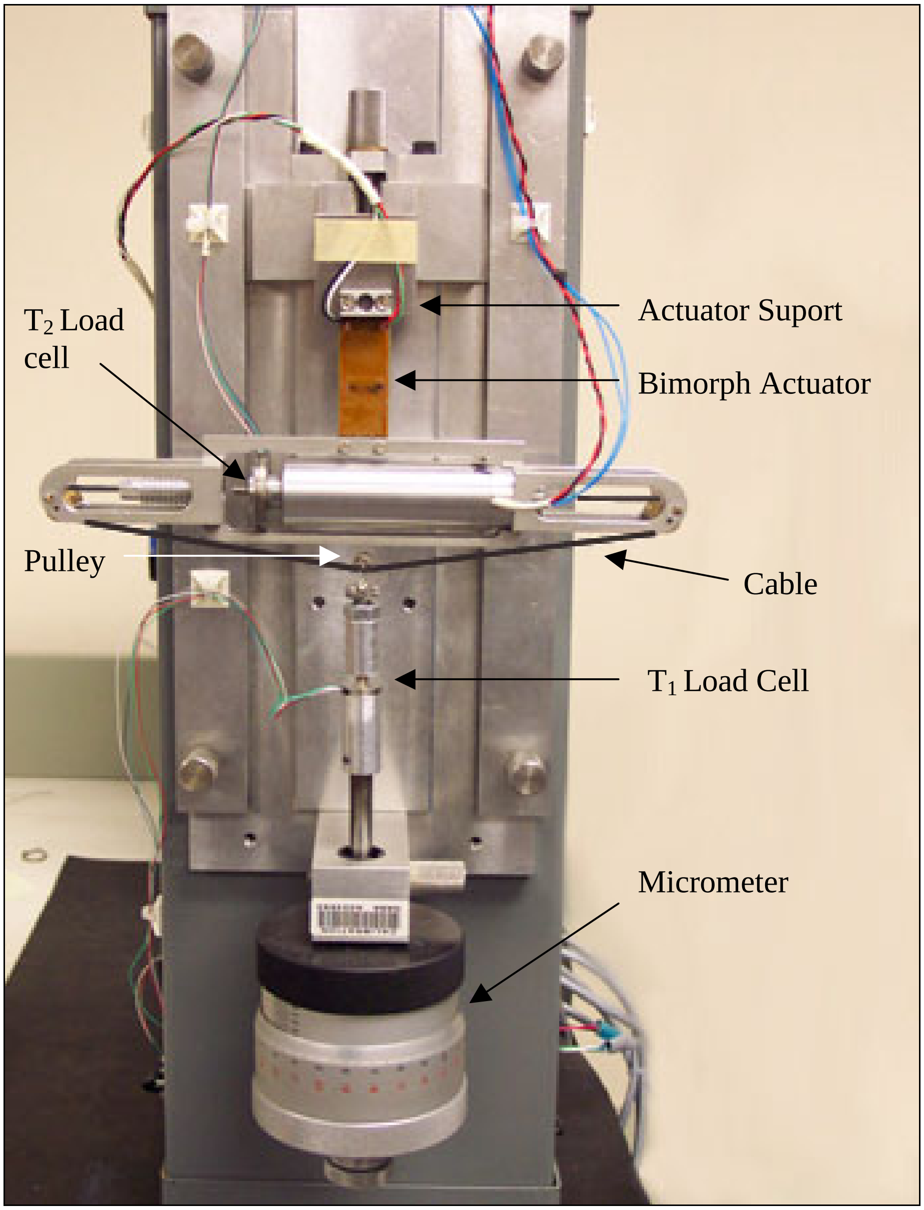

Figure 5.1 Bench test setup

The load cell at T_2 is rated to 100 lb (444.8 N) with a conversion factor of 256.4 mV/lb (57.6 mV/N) and a noise level of approximately 25 mV. This equates to an uncertainty in the measurement of about 0.1 lbs (0.444 N). The load cell at T_1 is rated to 50 lb (222.4 N) with a conversion factor of 552.8 mV/lb (124.3 mV/N). This load cell has a noise level of approximately 1.5 mV, corresponding to an uncertainty in the measurement of about 0.0027 lbs (0.0012 N).

Control and feedback signals for the testing of the actuator are processed through a dSPACE real time signal processor. Using dSPACE's ControlDesk software, the input and output signals for the actuator are tracked and stored for later analysis. Models of the system are built in Simulink® for each test, specifying proper input voltage levels and signal type as well as conditioning outputs.

Control signals to the bimorph part of the actuator are amplified using a Trek 50/750 high voltage amplifier. The Trek amplifier is capable of producing a 750 V output, though the maximum voltage specification for the piezo patches on the leaf spring is 500 V. Bimorph performance is measured using the Keyence laser displacement sensor, and an HP signal analyzer is used to compute the frequency response functions of the system. The laser displacement sensor is mounted on a tripod in front of the actuator fixture, with the laser aimed at the actuator housing, while the HP signal analyzer steps through a sine sweep between 1 – 200 Hz to develop an FRF for the piezo bimorph. The laser displacement sensor has an associated noise level of approximately 1 mV. Using the high accuracy mode, this noise level equates to a position error of approximately 0.0004 in (10.16 μm).

Control signals to the piezo stack part of the actuator are amplified using a custom amplifier built at NASA Langley Research Center. This amplifier is capable of a ±190 V output. However, the piezo stack is only driven between –30 V and +150 V.

Both load cells are powered by a 15 V supply, and the feedback signals from the load cell signals are processed through a Strain Gage Signal Conditioner. The signal from the stack load cell at T_1 has a gain of 10, whereas the load cell at T_2 has a gain of 100. The feedback signal from the laser displacement sensor is fed directly to the dSPACE system without any signal conditioning.

Actuator Results

Bench testing of the actuator includes the collection of data from the two piezo actuators and the understanding of how the actuator setup parameters influence performance. Actuator effectiveness is evaluated in terms of the in-plane tension control, the in-plane displacement control, and the out-of-plane deflection control.

The stack piezo provides the in-plane tension control and displacement. It is capable of motion in two directions, although the maximum displacement in both directions is not equal. Though the stack is considered to be bipolar, it cannot provide as much deflection in compression as it can in extension. Testing of the stack focused on unidirectional testing of the stack. The ability of the stack to maintain static displacements allows for testing to determine quasi-static membrane tension changes and membrane displacements.

Two voltage profiles were used in testing of the piezo stack. Initially, a staircase loading profile was used to test the tension control capability of the stack. The voltage profile to the stack ranges from 0 to 150 V in increments of 10 V. The profile is constructed to dwell 20 seconds at each voltage increment, which allows ample time for settling of the tension levels. The T_1 and T_2 load cells are monitored continuously and variations seen at either load cell are used to evaluate performance. The same staircase voltage profile is used for multiple tests with varying tension levels and cable angles.

A second test was run using the piezo stack, with an increasing step input voltage profile. This profile steps through the voltages from 0 to 150 V in increments of 10 V. However, after each increment the voltage is allowed to drop back to zero. The period for the increasing step profile was 6 seconds. This test was performed to quantify any difference between a gradual loading profile and a large step profile.

The performance of the stack is measured through the outputs of the T_2 load cell, the in-line load cell T_1, and the micrometer. The cable angle can be determined by using the geometry of the cable setup and the ratio of the output of the load cells. Data from both load cells and the input data to the stack are stored for later evaluation.

Testing of the bimorph piezo is performed using an HP signal analyzer and a Keyence® laser displacement sensor. Frequency response functions of the bimorph are recorded with the HP signal analyzer using a sine sweep function from 1 to 200 Hz. The same input is used for various tension levels. The purpose of the increasing membrane load levels is to determine how the performance characteristics of the actuator vary with increased loading.

In-Plane Testing

For the in-plane testing, there are three dominant coupled factors that determine performance of the piezo stack: the cable angle (θ), the change in tension (ΔT_m), and the deflection of the membrane attachment point (δM). During initial bench tests several inconsistencies in the performance of the in-plane actuation mechanism were apparent. Testing has shown that a tension differential develops in the cable between the T_2 load cell and the T_1 load cell. This is likely due to friction around the pulley. With high pre-tension loads in the cable, and high loads placed on the pulley, friction in the pulley increases and hampers performance. Performance degradation due to friction is seen in the tests that monitor the tension and deflection of the membrane.

Figure 5.2 is a typical load profile plot for the staircase test. The plot shows the response from both the T_1 and T_2 load cells for a configuration with the cable angle of 12 degrees. Results show that when the piezo stack is in operation, using comparable membrane load tension levels and cable angles as for the membrane test bed, the stack was only able to obtain a ΔT_m of approximately 0.15 lbs (0.667 N). The change in cable tension ΔT_c is approximately 1.2 lbs (5.338 N).

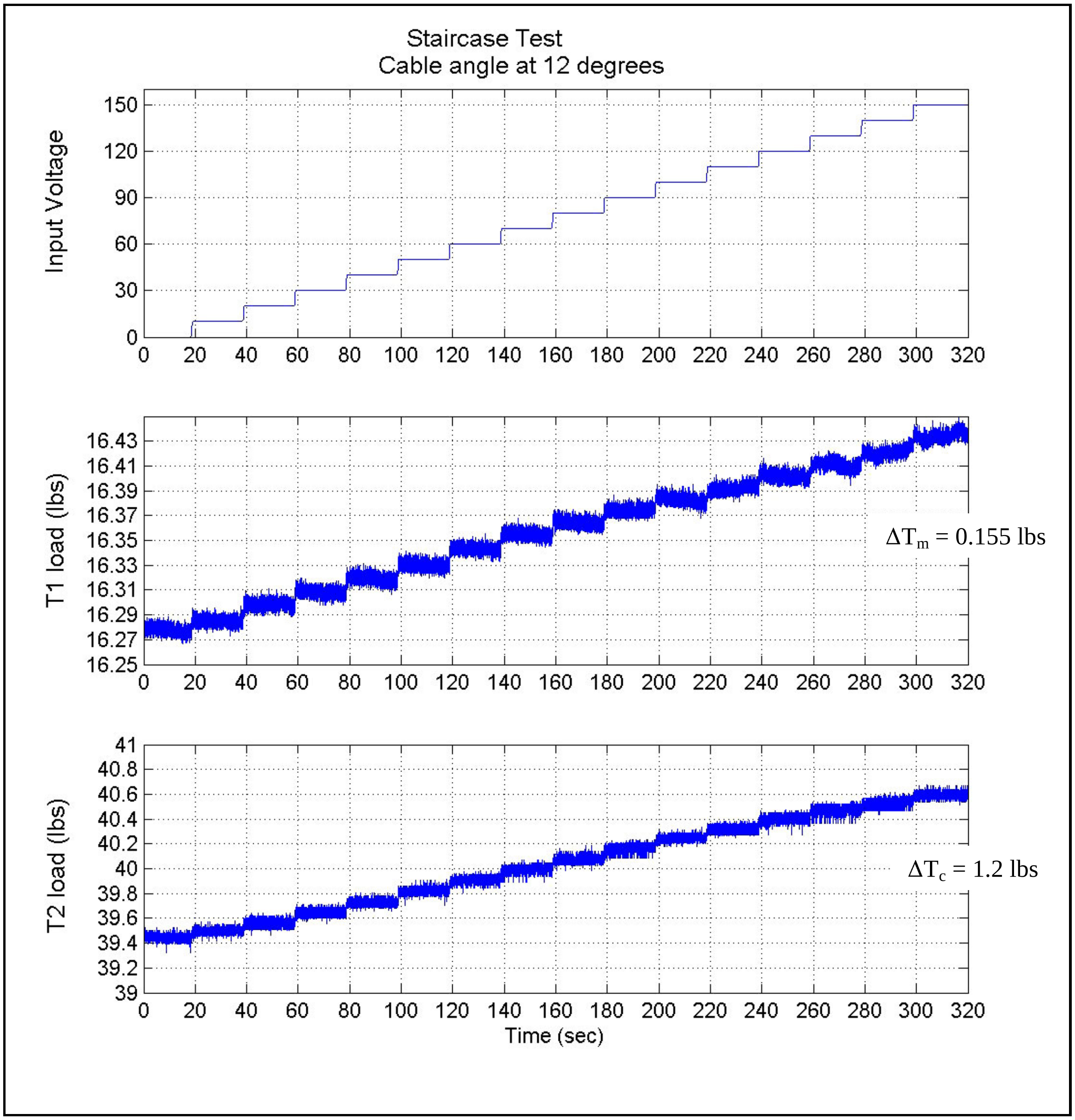

Figure 5.2 Staircase profile for in-plane tension adjustment at 12˚ cable angle

To compute the initial cable angle, solve Eq. 3.15 for the angle

$$\theta_1 = \sin^{-1}\left(\frac{T_m}{2\cdot T_c}\right) = \sin^{-1}\left(\frac{16.278}{2\cdot 39.475}\right) = 11.89^\circ \qquad 5.1$$

Values for T_m and T_c are average values in the desired region. Similarly, the ending angle is

$$\theta_2 = \sin^{-1}\left(\frac{16.435}{2 \cdot 40.59}\right) = 11.68^\circ \tag{5.2}$$

Using the specified maximum deflection of the piezo stack of 0.00252 in (64 μm), the starting cable angle, and the deflection geometry using a calculated value for L/2 of 5.34 in (135.6 mm), the minimum expected deflected angle can be calculated using equation 3.17 in the form

$$\theta_2 = \cos^{-1}\left(\frac{5.34}{\frac{5.34}{\cos(\theta_1)} - \frac{0.00252}{2}}\right) = 11.83^\circ \tag{5.3}$$

Figure 5.3 shows the response for the same input, but at a 9˚ cable angle. At the smaller angle, the change in tension at T_1 is approximately 0.30 lbs (1.334 N). The tension at T_1 changed approximately 0.85 lbs. This demonstrates a marked improvement in achievable tension from the same profile at a larger angle, and it also shows the expected increase in tension adjustment capability at lower cable angles. It is important to note that the initial tension load is lower for the 9˚ data set, which may contribute to the difference. Friction losses may not be as significant in this case.

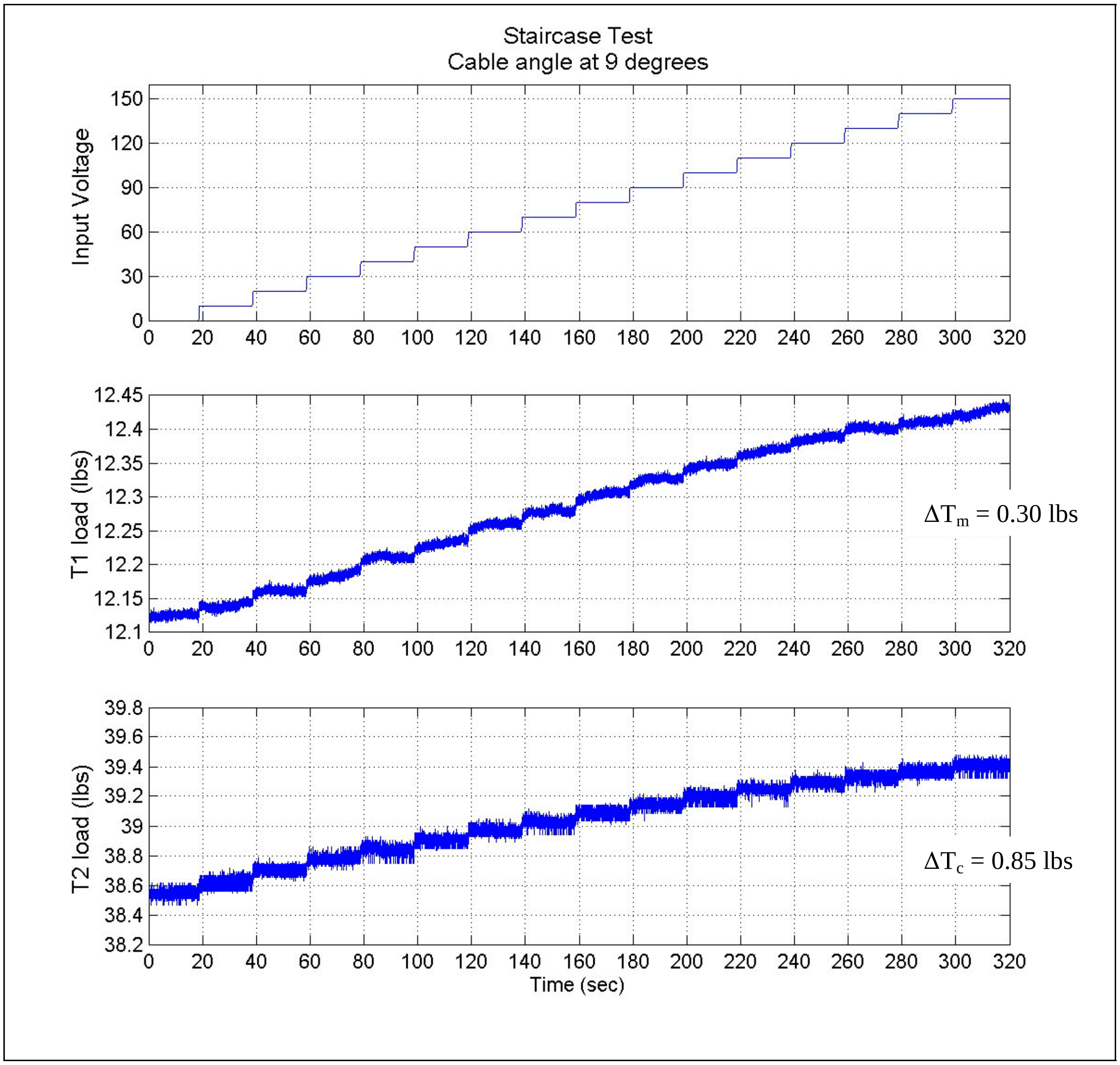

Figure 5.3 Staircase profile for in-plane tension adjustment at 9° cable angle

Using Eq. 5.1, the initial cable angle can be determined using the data from the load cells as

$$\theta_1 = \sin^{-1}\left(\frac{12.125}{2 \cdot 38.54}\right) = 9.05^\circ \qquad 5.4$$

Using the final tension value, the measured final angle can be determined as

$$\theta_2 = \sin^{-1}\left(\frac{12.425}{2\cdot 39.42}\right) = 9.06^{\circ} \qquad 5.5$$

Once again, this value does not seem appropriate. Due to a shortening of the stack, there should be a decrease in cable angle rather than an increase. Using Eq. 5.3 and inserting the appropriate values for θ_1 and a calculated L/2 value of 5.93 in (150.6 mm), the minimum expected deflected angle can be calculated to be

$$\theta_2 = \cos^{-1}\left(\frac{5.93}{\frac{5.93}{\cos(\theta_1)} - \frac{0.00252}{2}}\right) = 8.97^{\circ} \qquad 5.6$$

The discrepancy between the calculated minimum angle and the test results for both test cases, and the unexpected increase in angle for the 9º test case, indicates a problem with the cable mechanism. It is also important to note that the profile for the T_2 load with the 9˚ cable angle is not linear. The rate of change in tension decreases at the higher loads. As with figure 5.2, the profile of the tension load at T_1 is inconsistent and does not stay constant at each step. Fluctuations in the load profiles may be due to a lack of cable tension equilibrium on either side of the pulley.

The cable setup, while offering a mechanical advantage at small cable angles, also introduces friction into the system, which creates a tension differential in the cable on either side the housing pulley. From this data it is clear that cable angle cannot accurately be determined by the load cell data. More importantly, the tension at T_2 does not provide an accurate representation of the tension value at T_1. Variability in actuator setup such as cable pre-tensioning and cable angle exerts strong influences in the friction levels and makes it difficult to know *a priori* what the friction coefficient is at the pulley. This is important because when the actuator is connected to a membrane, the only load cell in place will be T_2. The membrane tension load is only observable by the cable tension at the stack, which does not necessarily match the cable tension on the membrane side of the pulley.

The bench test setup allowed for measurement of displacement at the membrane attachment point. This information shows that at operational tension levels there is a loss of displacement transmission between the piezo stack and the membrane attachment point. Figure 5.4 shows the load profiles for a test in which the piezo stack is commanded a voltage while the micrometer is adjusted to return the tension load read at T_1 to its nominal "zero voltage" value. In the absence of friction, this test provides an alternate means to determine elongation of the stack

Figure 5.4 also shows that after zeroing the tension load at T_1, the cable tension at T_2 increased 1.3 lbs (5.783 N). Maximum δM of the membrane attachment point for these tests was approximately 0.0022 in (55.88 μm). To avoid problems with dead band in the micrometer, the displacement adjustments were always made by turning the micrometer in the same direction. This accounts for the spikes in both directions in the T_1 load profile. Tension adjustments at T_1 are not noticeable at T_2, and are in the noise floor for the load cell.

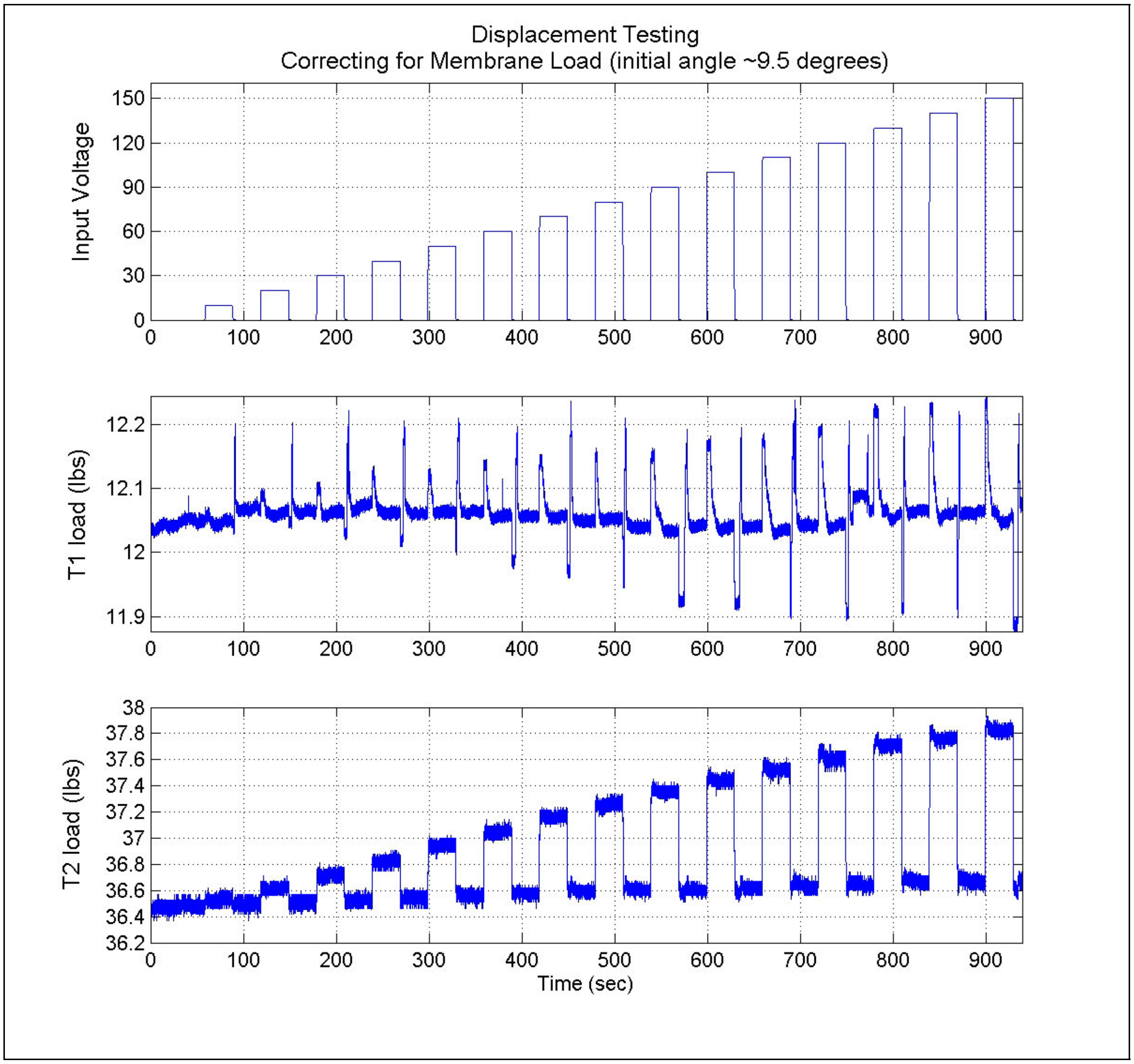

Figure 5.4 Displacement test correcting for membrane load

Similar tests zeroing the load cell at T_2 rather than T_1 resulted in δM of approximately 0.027 in (685.8 μm). In order to maintain a constant cable tension, the change in tension at T_1 for these tests was approximately 2 lbs (8.896 N). These results verify that the load cell at T_2 has a dead band of 2 lbs, and therefore tension in a membrane assessed from T_2 has an error of ±2 lbs (8.89 N). Testing has shown that the capability of the piezo stack to change tension in the membrane is less than 0.5 lbs (2.22 N). This change is smaller than the error, which makes it impossible to accurately measure membrane tension change.

For comparison, the same profile can be seen in figure 5.5 without any displacement adjustments. Looking at the tension load T_1 during the time intervals when the input is zero reveals that the tension value changes. This helps point out the fact that the tension values do not return to a steady state, indicating that there are other forces acting on the system.

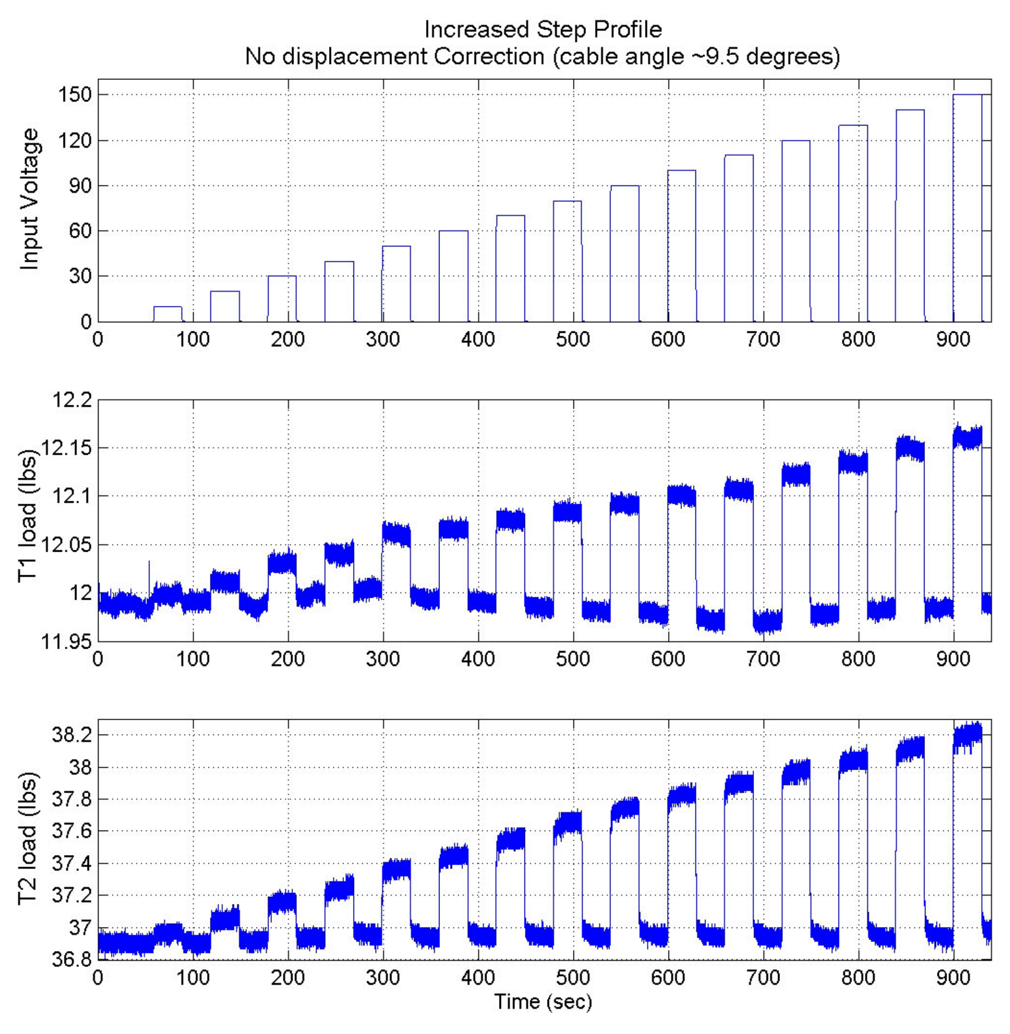

Figure 5.5 Increased step testing with no change in displacement from micrometer

Figure 5.6 compares the results from the bench test to the results from the analysis. In this figure, the staircase profile is plotted for the bench test, along with the expected results from the analysis. The analysis results are normalized to have the same starting point as the bench test. The expected final T_1 tension load is greater than the actual load by approximately 0.10 lbs (0.445 N), and the expected T_2 tension load is less than the actual tension load by approximately 0.22 lbs (0.978 N). The overall results correlate relatively well at this cable angle and tension, with a slightly larger divergence of results at the higher tension levels.

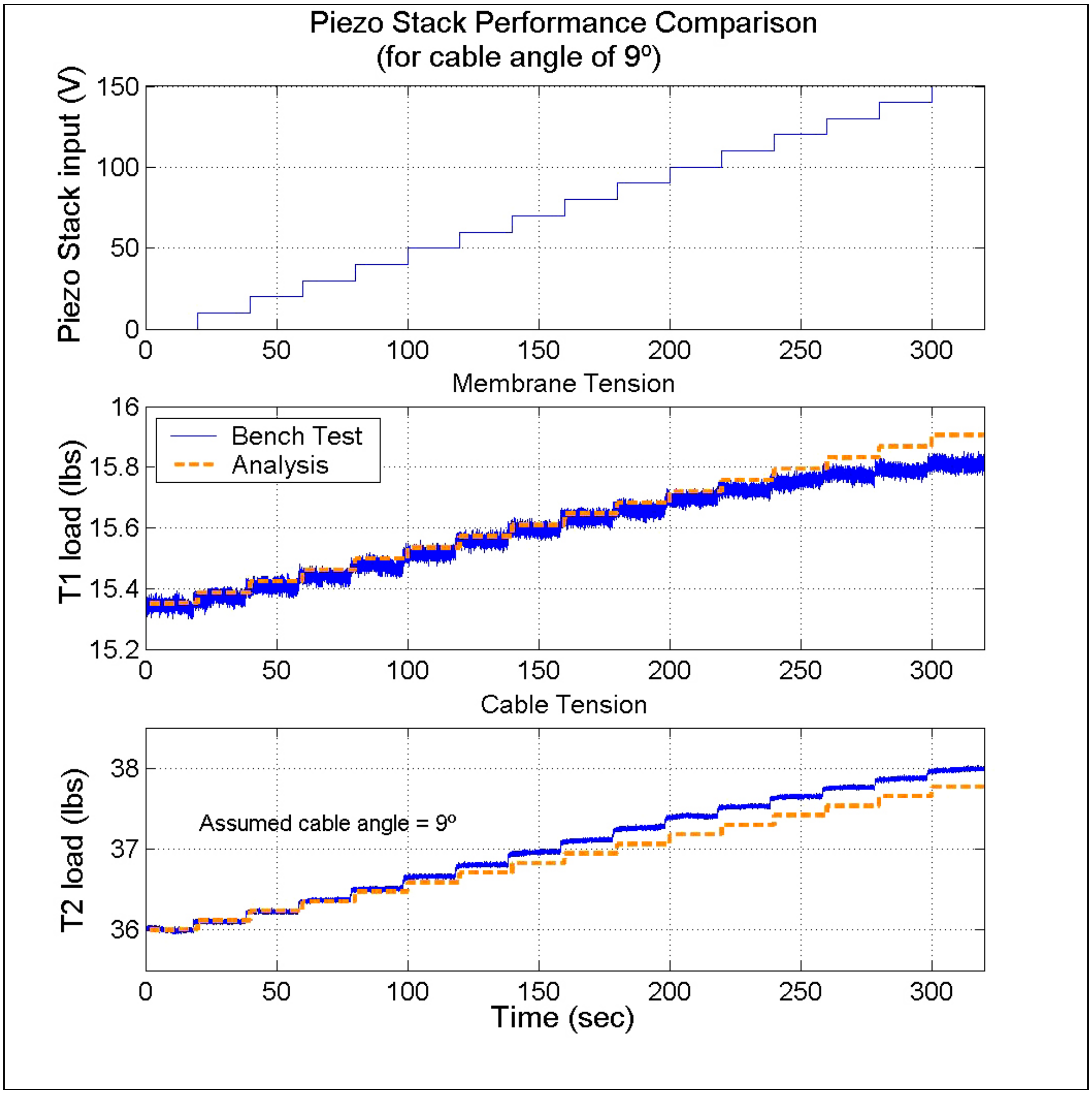

Figure 5.6 Bench test and analysis results correlation for 9º cable angle

Figure 5.7 shows the same profile with a larger cable angle and a higher tension level. The T_1 results for this profile do not match well with the expected results. The expected final value for the T_1 load is approximately 0.30 lbs (1.334 N) greater than the actual value. The expected change in tension is 0.47 lbs (2.091 N), where the actual change in tension is only 0.17 lbs (0.756 N). Despite the lack of correlation between analysis and bench test for the T_1 load, the T_2 load is a much closer match. The error between analysis and test for the T_2 load is only 0.08 lbs (0.356 N).

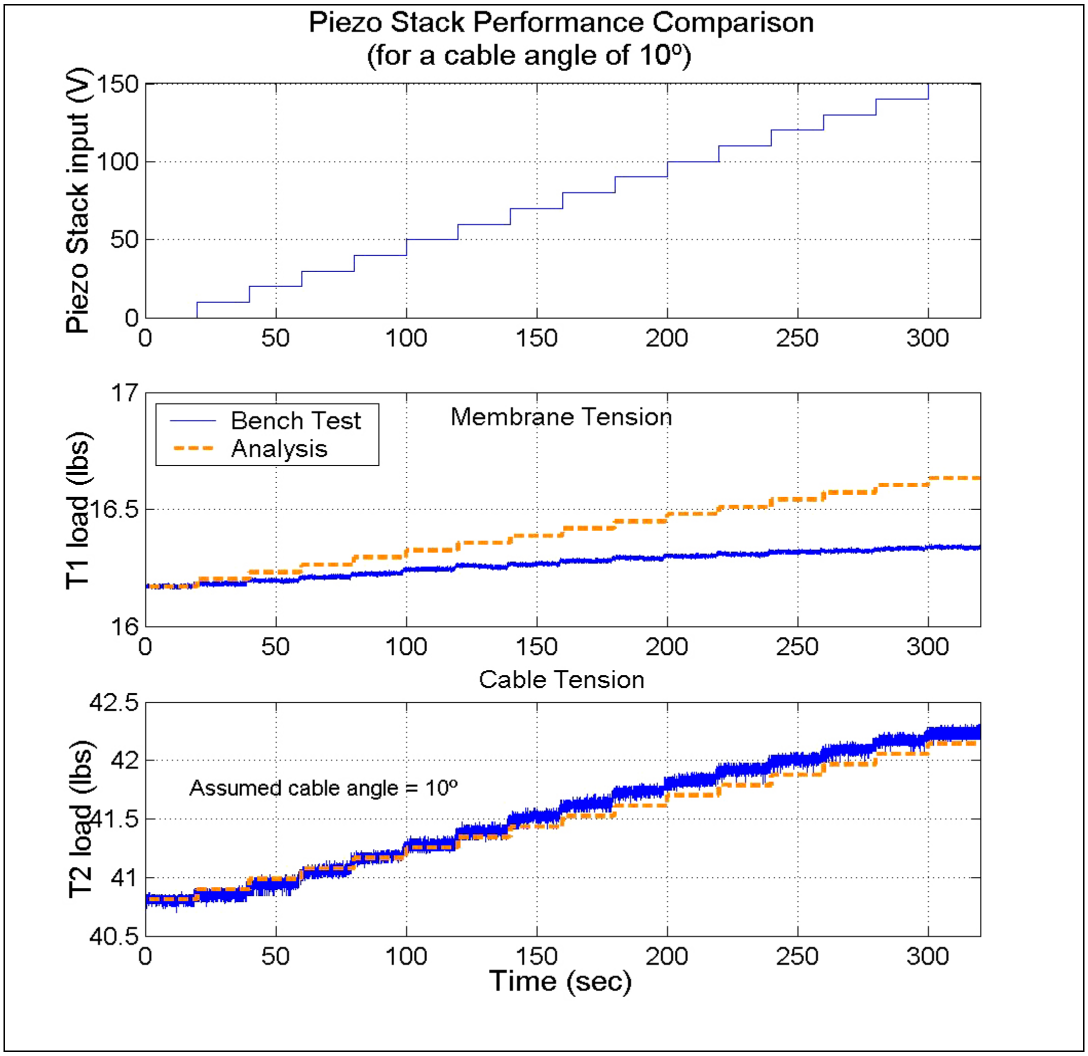

Figure 5.7 Bench test and analysis results correlation for 10º cable angle

While some of the bench test data can be correlated to the analysis to show good results, the test data are somewhat inconsistent and highly variable depending on pre-tension levels and cable angle. Tests run at the same cable angle with different pre-tension levels have varying results. The 2-D simulation incorporates cable angle and pre-tension as constant gain values and does not allow for variation of the cable angle, which occurs during actuator operation.

Out-of-Plane Actuator Performance

Testing of the out-of-plane capabilities of the actuator focuses on the piezo bimorph. In order to determine performance of the bimorph actuator, frequency response functions were taken with the actuator under different tension loads.

The FRF for the piezo bimorph out-of-plane displacement as a function of input voltage for tension loads of 0 and 0.2 lbs is shown in figure. 5.8. For this FRF, the laser displacement sensor was used to provide output, and input is the voltage signal to the piezo bimorph. A dominant resonance at 7 Hz is seen for the no tension load case. Further testing reveals that this peak contains two fundamental modes of vibration for the bimorph and actuator housing. Both first bending and the first torsion modes coalesce within the single peak. When a tension load is applied at T_1, the two modes split, revealing both modes. Stiffening of the bimorph due to applied tension loads causes an increase in bending frequency. The torsion mode is unaffected by the loading because the point load at the pulley is in line with the center of the bimorph, and therefore does not add any torsional stiffness. The torsion mode remains at approximately 7 Hz. In order to see the torsion mode, the laser displacement sensor is pointed at a point on the housing, approximately 1 in (2.54 cm) to the right of center.

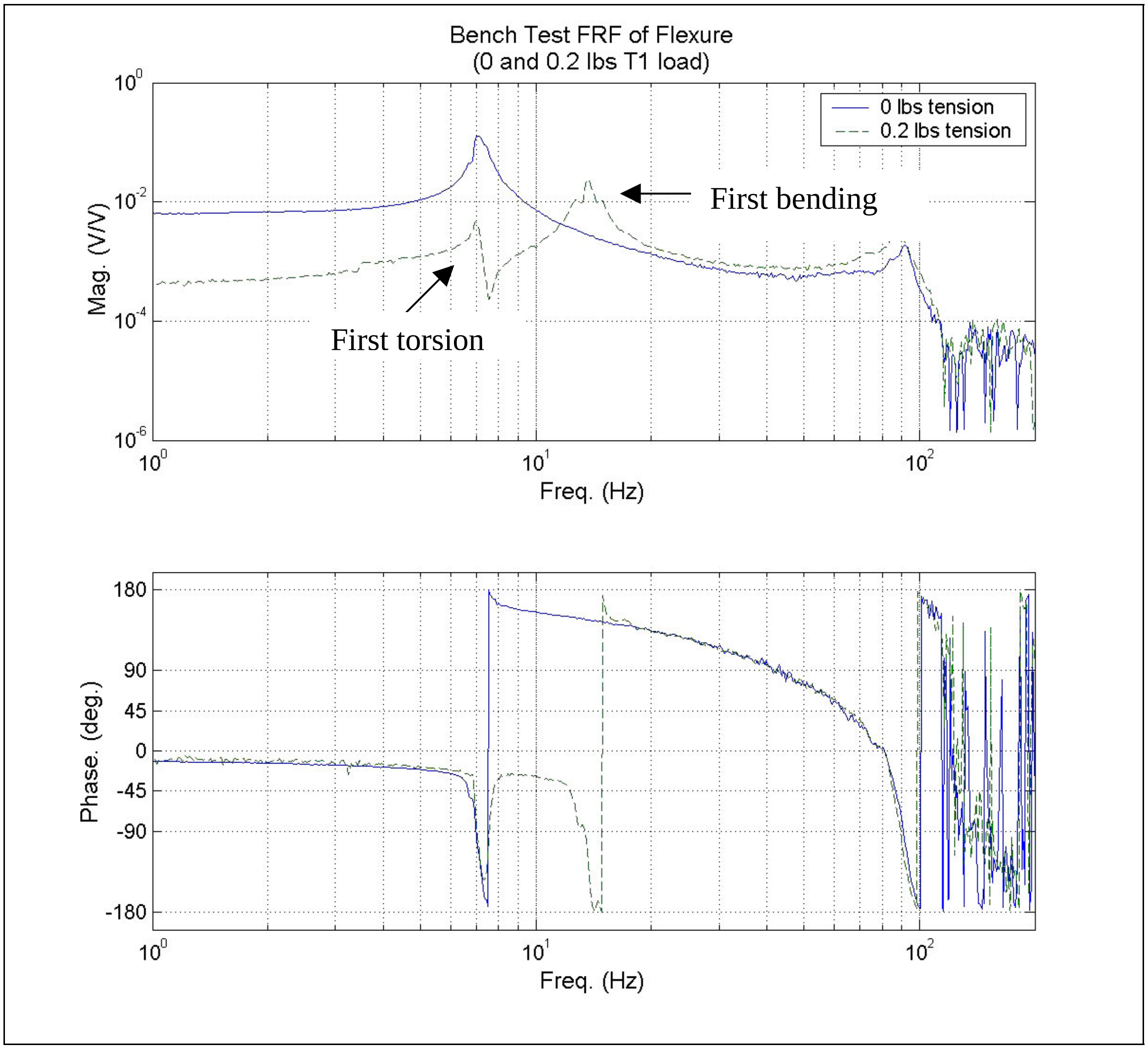

Figure 5.8 Bench test FRF results showing effect of increased membrane tension

The laser displacement sensor can be positioned at the center of the actuator, which effectively disables the ability of the sensor to sense torsion. This helps to isolate the characteristics of the bending mode under different loading conditions. Figure 5.9 shows the magnitude response of the actuator and the migration of the first bending mode frequency with higher tension load. The same output/input configuration is used for this FRF, with the laser displacement sensor providing the output signal, and input is the voltage to the piezo bimorph. As the loading is increased, the bending mode frequency changes at a rate of approximately 2.5 Hz/lb (0.562 Hz/N). The second peak shows the second bending mode, also affected by the increased tension. The rate of migration of the two peaks is not equal, and leaves some room for speculation as to why.

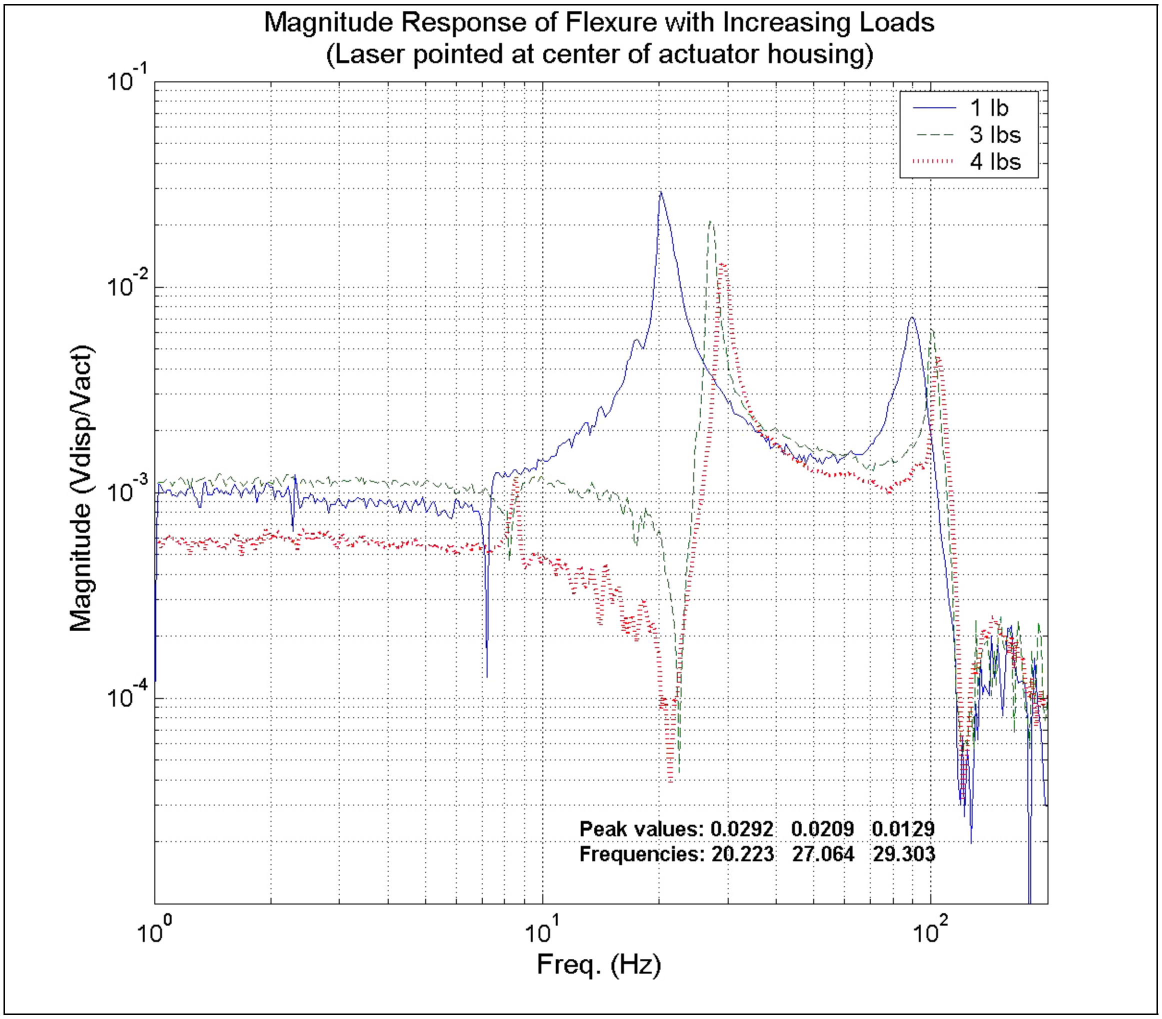

Figure 5.9 Magnitude response of actuator with increasing load up to 4 lbs

Also noticeable from the FRF figures is the significant drop in magnitude at low frequencies with only a small tension load. Further testing show that at tension levels higher than 4 lbs (17.8 N) the off resonance magnitude is significantly lower than the no tension case. No data are collected for the high-tension case because the response is within the noise floor of the displacement sensor. Essentially, the piezo bimorph seems ineffective at higher tension loads.

Based on the results from the bench tests, the out-of-plane deflection capability of the actuator at zero tension load is equal to approximately 0.00258 in/100 V (646 µm/100V), with a maximum voltage to the bimorph of 450 V. This results in a maximum out-of-plane deflection of 0.0116 in (294 µm). With loading, the out-of-plane deflection capability is significantly decreased. Figure 5.10 shows bench test results for out-of-plane deflection as a function of tension load. Deflection values for loads above 4.0 lbs (17.792 N) are not reliable, and therefore are not included.

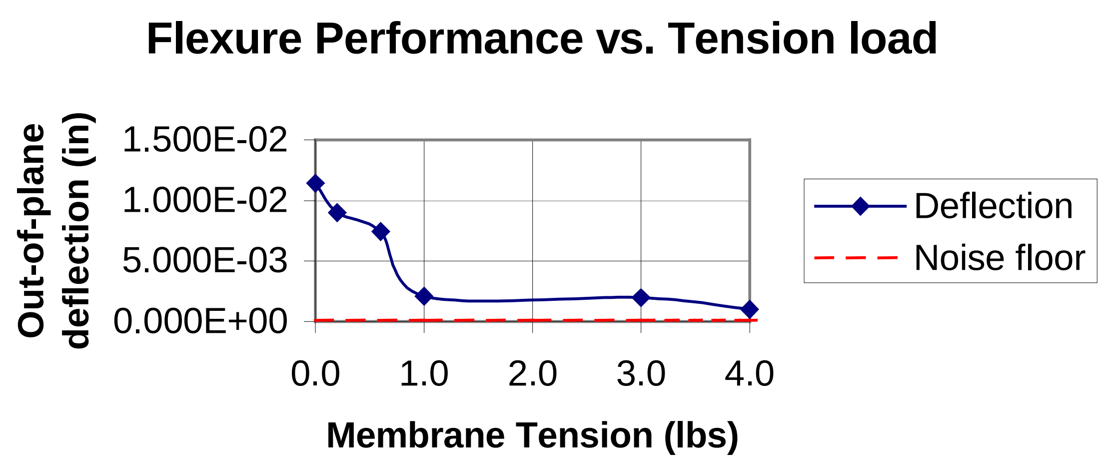

Membrane Tension	Out-of-plane Deflection
0.0 lbs (0.000 N)	1.144E-02 in (290.70 mm)
0.2 lbs (0.890 N)	9.009E-03 in (228.83 mm)
0.6 lbs (2.669 N)	7.441E-03 in (189.00 mm)
1.0 lbs (4.448 N)	2.096E-03 in (53.24 mm)
3.0 lbs (13.344 N)	1.977E-03 in (50.22 mm)
4.0 lbs (17.792 N)	1.026E-03 in (26.07 mm)

Figure 5.10 Membrane tension load and out-of-plane deflection capability of bimorph

Figure 5.11 shows a comparison of the FRF's from the bench test and the linearized model of the system at a T_1 tension load of 0.2 lbs. The profiles for both test and analysis have similar contours, though the location of some of the peaks is shifted. The first torsion mode peak for the analysis is 3 Hz higher than for the bench test results, and the frequency of the first analytical bending mode peak is 4 Hz higher than for the bench test results.

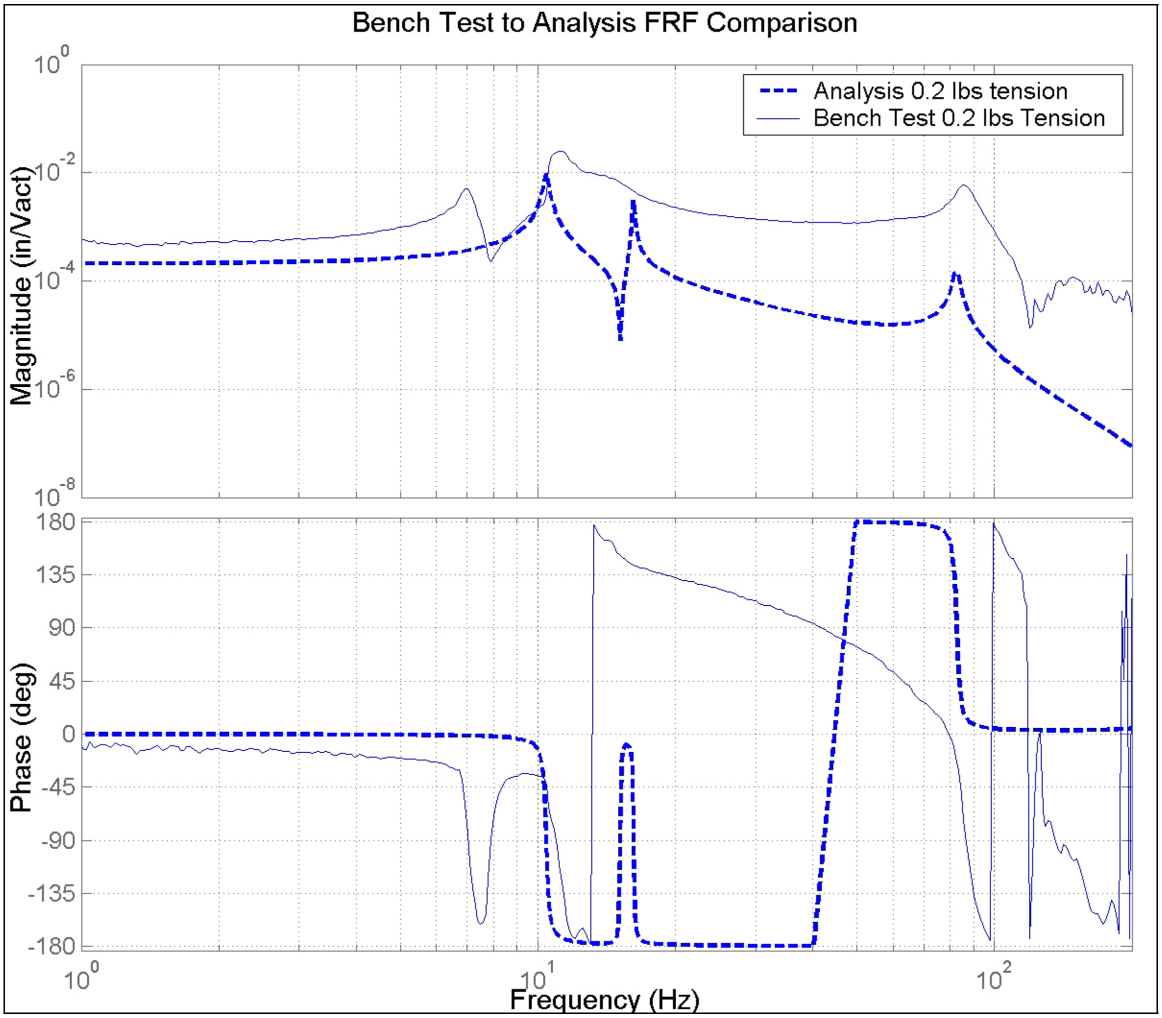

Figure 5.11 FRF comparison of bench test to analysis for a 0.2 lb load situation

Figure 5.12 shows the same comparison of analysis to bench test at 4 lbs tension. The data for this graph were taken at the center of the actuator, so the torsion mode is not noticeable.

The first bending mode peak for the analysis is now lower in frequency than the bench test results by approximately 8 Hz. Based on the results of figures 5.11, and 5.12, it is possible that the bench test has a much higher stiffness coefficient than used in the analysis, which may account for the discrepancies in peak frequencies.

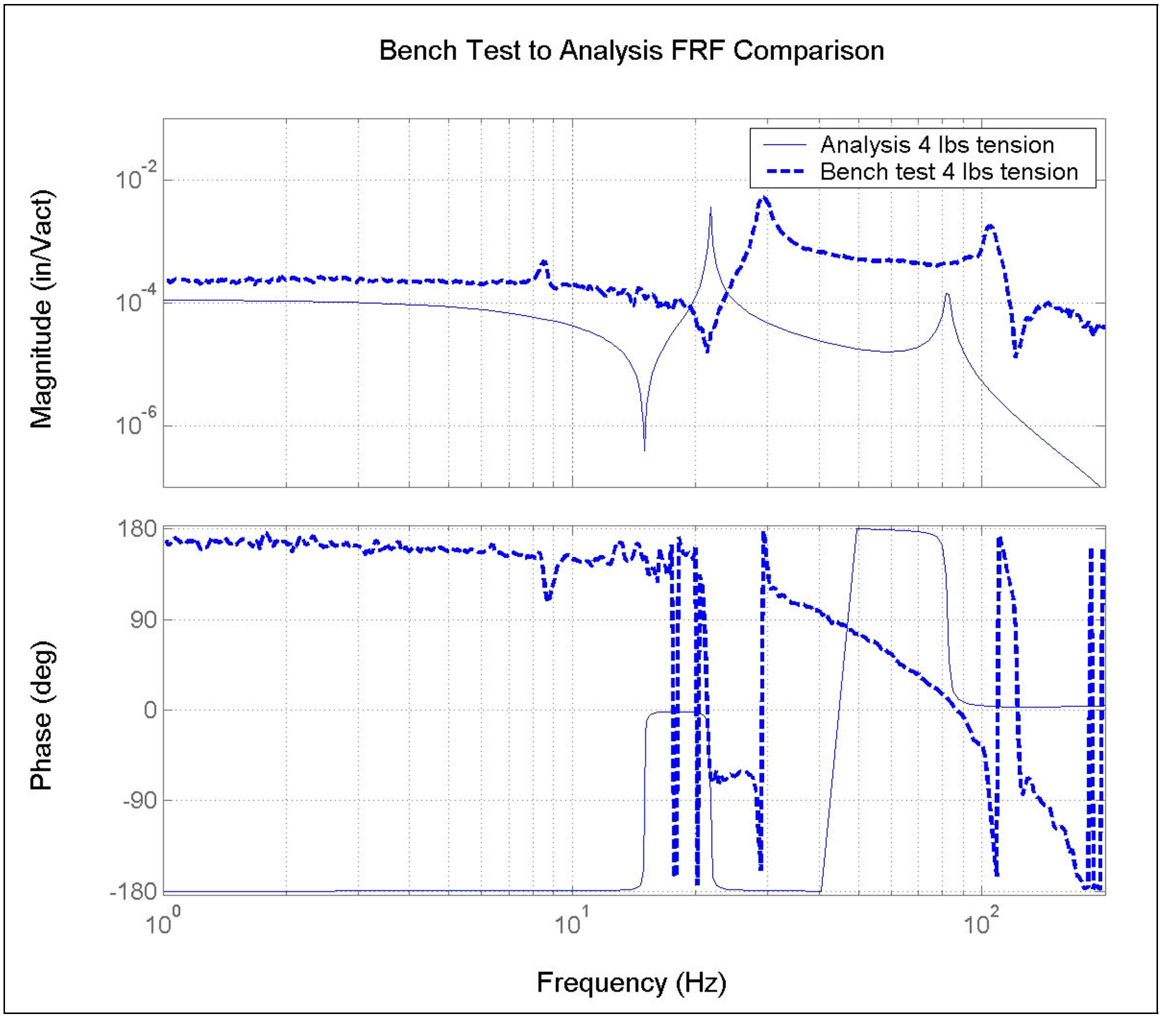

Figure 5.12 FRF comparison of bench test to analysis for a 4 lb load situation.

Note the change in frequency of the second peak, which rises in frequency in the bench test. However, it remains constant in the analysis. This peak is believed to be a second bending mode peak, which is evident in the bench test results. The poor correlation of these two peaks is a subject for further investigation. The offset between analysis and test, for both examples, points towards differences in stiffness values in the model of the piezo bimorph or the assumed equivalent spring constants for the membrane and further work can be done to better correlate the analysis to the bench test setup.

MEMBRANE TEST

Setup

For evaluation of the actuator with more realistic boundary conditions, the actuator was installed in the hexapod structure shown in figure 2.1. It replaced one of 12 cables used to stretch the membrane. After installation the actuator is configured as shown in figure 5.13. The bimorph actuator is attached to a bracket bolted to one of the twelve coupling joints of the torus. The membrane edge is equipped with a hard plastic attachment point containing a pulley for the actuator cable to pull against. The membrane is tensioned at each of the attachment points at a nominal tension of approximately 16 lbs (71 N). However, tension applied to the membrane with the actuator in place to approximately 14 lbs (62 N). The slightly lower tension level at the actuator is used because of difficulty turning the tension adjustment screw and clearance between the actuator housing and the membrane pulley.

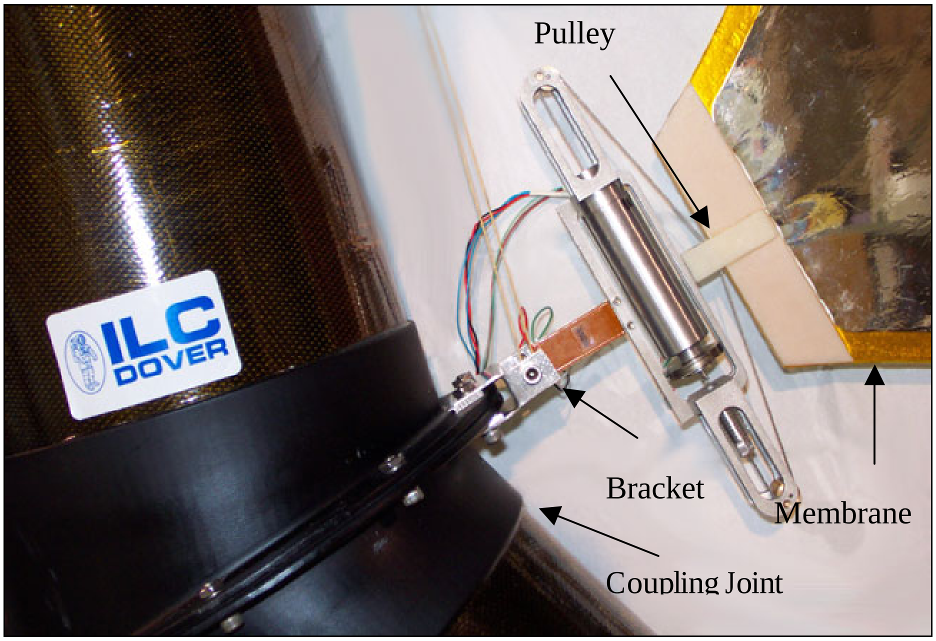

Figure 5.13 Actuator connected to membrane

An Ohmetron® laser vibrometer and a Keyence® laser displacement sensor are used to measure out-of-plane velocity and displacement, respectively, at various points on the membrane and actuator. For initial testing, 14 test points are mapped out on the membrane to form a wedge shaped region about the actuator as shown in figure 5.14. The first four points cover the actuator housing, the pulley, the plastic brace, and the edge of the Kapton material. Other points run radially from the center of the actuator, and from the catenaries on either side of the actuator, to the center of the membrane. The bimorph actuator is driven with a ± 390 V random noise signal and the laser displacement sensor is used take FRF data at all 14 points.

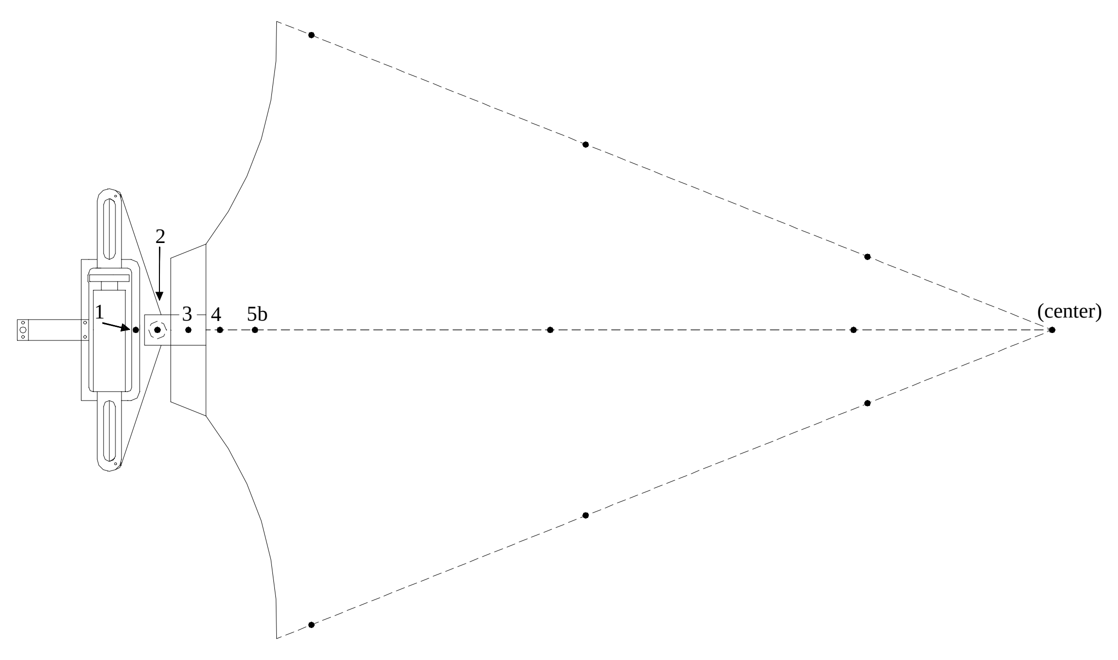

Figure 5.14 Membrane scan points (picture not to scale)

Membrane Test Results

Piezo Stack Actuator Excitation

Testing of the in-plane capabilities of the actuator confirms the inability of the piezo stack actuator to affect tension. Therefore, most of the membrane test concentrated on the out-of-plane behavior of the system.

Piezo Bimorph Actuator Excitation

Figures 5.15 and 5.16 show the setups for testing of the bimorph with the laser vibrometer and displacement sensor respectively. Both setups show the laser pointed at the pulley.

Figure 5.15 Laser vibrometer setup

Figure 5.16 Laser displacement sensor setup

Initial piezo bimorph tests show the ability of a single actuator to produce visible motion in the membrane. In testing of the bimorph actuator control authority, it is clear that it has a very large bandwidth. From top to bottom of figure 5.17 are the magnitude, phase, and coherence responses using the laser vibrometer. FRF data collected with the HP analyzer and the laser vibrometer pointed at the membrane pulley show dominant peaks around 15 Hz, 100 Hz and 1 kHz. The laser vibrometer has a bandwidth of approximately 25 kHz, but data above 3 kHz have poor coherence.

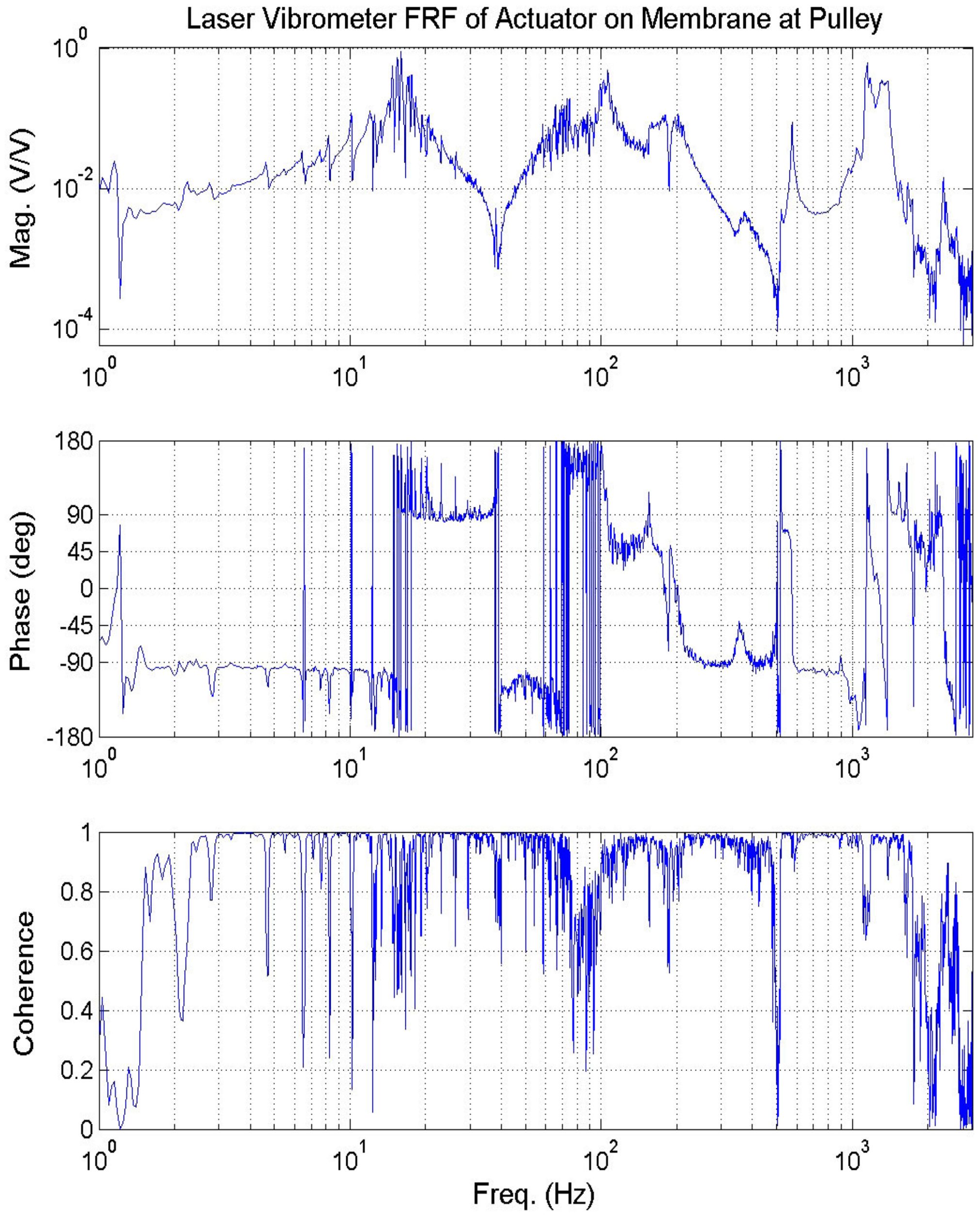

Figure 5.17 Laser vibrometer FRF at pulley

The FRF data is from a laser vibrometer pointed at the pulley of the membrane with a bandwidth limited random noise voltage input of 0.1 to 5 kHz to the piezo bimorph. Although not apparent from the data, there are hundreds of membrane modes contained in the 0 to 20 Hz range. Because of the near collocation of the sensor actuator pair, each resonant peak is followed by a zero, making identification of modes difficult.

Figure 5.18 shows data taken at the same point using the laser displacement sensor, which shows peaks in response at similar frequencies as in the data taken at the same point using the laser vibrometer. For this FRF a bandwidth limited random noise signal from 0.1 – 200 Hz input was applied to the piezo bimorph with the laser displacement sensor pointed at the membrane pulley providing the output signal.

The range of the response plot for the displacement sensor is smaller due to the significantly smaller operational bandwidth of the laser displacement sensor. Coherence begins to drop significantly at frequencies above 30 Hz. Low signal to noise ratio in the region above 30 Hz may be the cause of poor coherence. Both sensors have poor coherence below 3 Hz, and the bimorph actuator is known to have difficulty operating at low frequency ranges.

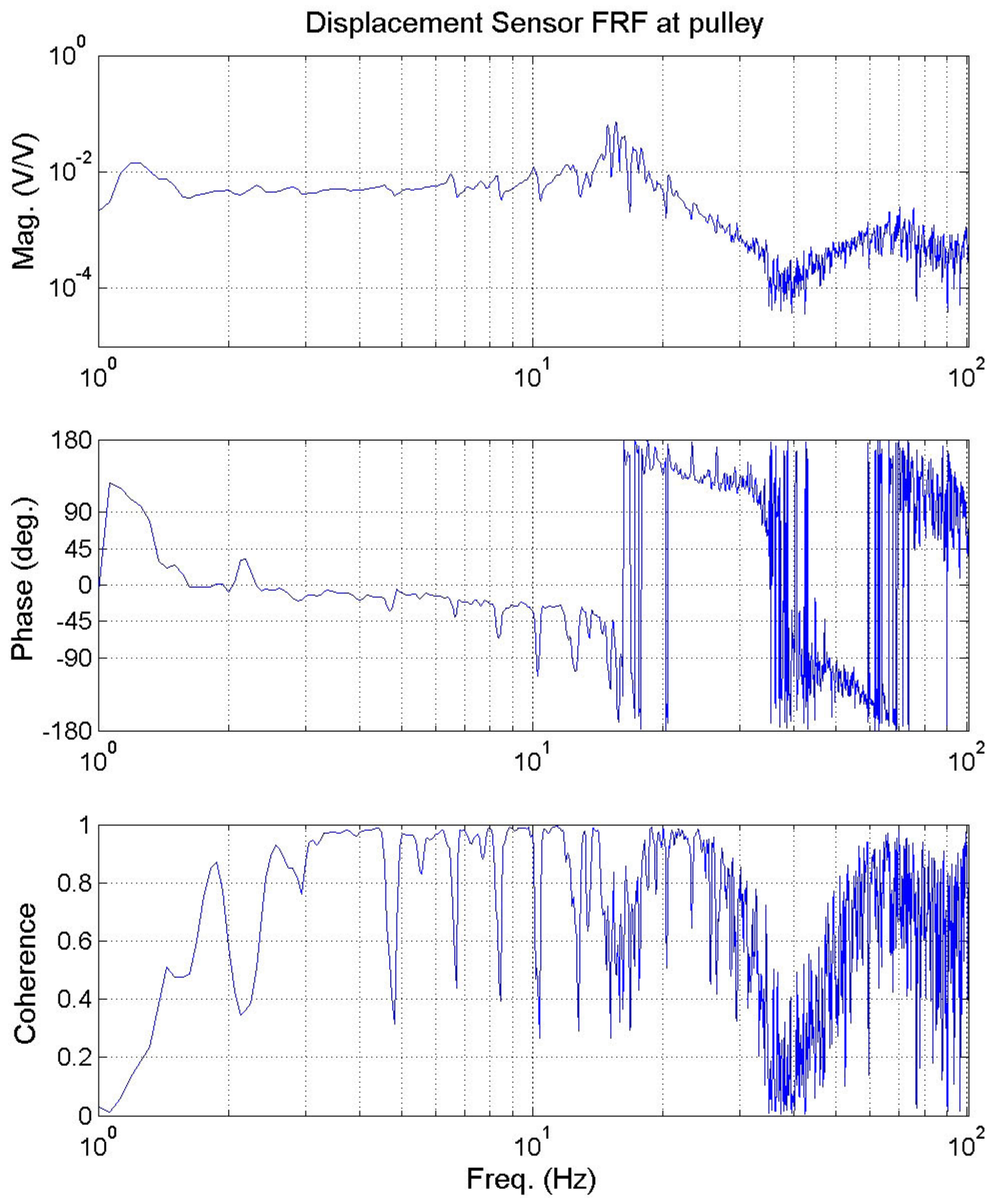

Figure 5.18 Laser displacement sensor FRF at pulley

Data taken at other points on the membrane show similar resonant peaks to those seen at the pulley, with more exaggerated peaks between 4 and 10 Hz. Figure 5.19 shows data for location 2 (top), 4 (center), and 5B (bottom) (refer to figure 5.14 for location points). The quality of data, in terms of coherence (not shown), diminishes as the sensor is moved away from the actuator.

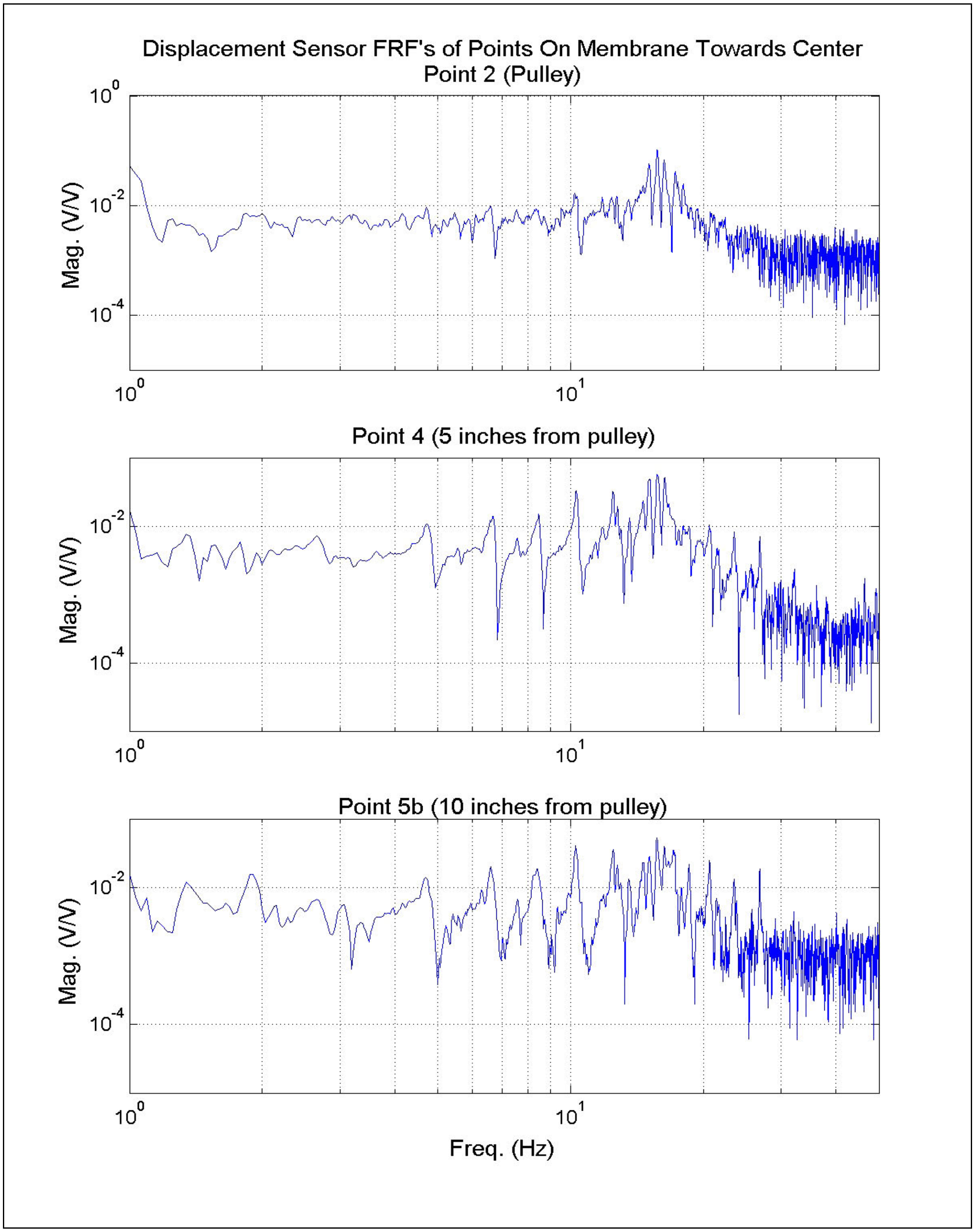

Figure 5.19 Displacement sensor FRF's at points located radially

Shaker Excitation

To study disturbance transmissibility across the actuator interface, a linear dynamic shaker is attached to the front side of the torus to provide an external disturbance input. The frequency response from the shaker input to the laser displacement sensor at location 2 on the pulley is shown in figure 5.20. FRF data shown are the result of a sine sweep from 0.1 - 25 Hz input to the shaker, using a laser displacement sensor pointed at the pulley for an output signal. Data from this test will be used to assess actuator control effectiveness later in the thesis.

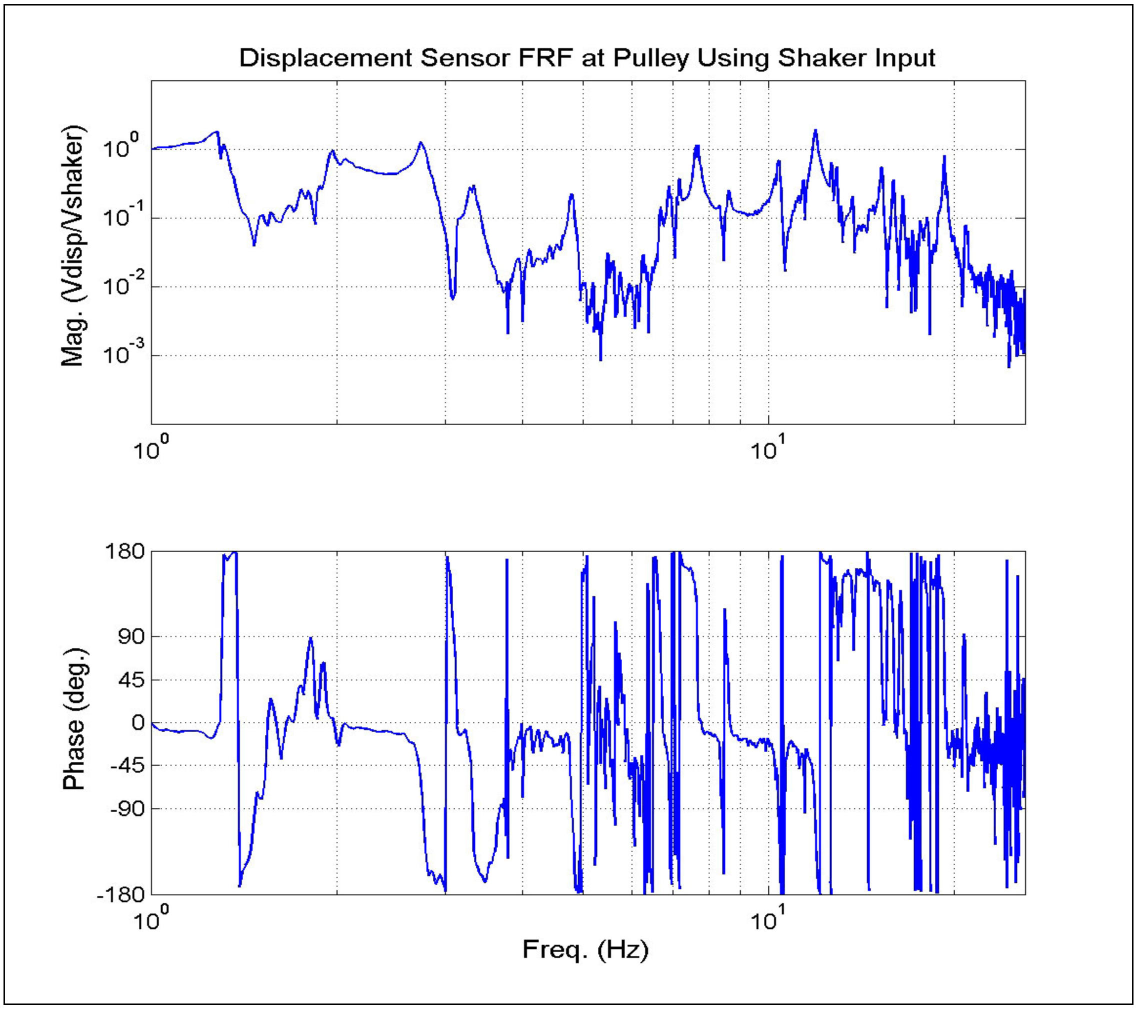

Figure 5.20 Displacement sensor FRF at pulley using shaker input on torus

Testing showed that the piezo bimorph had little effect on the membrane at frequencies below 10 Hz. The only frequency range the actuator is able to affect is between 10 and 20 Hz.

Chapter 6

ACTUATION AND CONTROL OF MEMBRANE

Closed Loop Feedback

A single actuator was capable of imparting visible motion in the large membrane. Based on the results from the test of the bimorph actuator on the hexapod, control of the membrane using the bimorph actuator shows potential. To demonstrate membrane controllability, a control problem is formulated using the shaker as an external disturbance and the membrane actuator to reduce disturbance propagation across the boundary.

Two sensors are evaluated for feedback control, a laser vibrometer and a laser displacement sensor. At first, velocity data seemed best from a control viewpoint, but after evaluating the FRF, it was discarded for several reasons. First, the high bandwidth of the vibrometer allows observation of resonant peaks throughout the frequency range up to 1 kHz. Secondly, high frequency noise from the vibrometer drives the piezo bimorph. Finally, because the sensor measures velocity, the output amplifies high frequency signals making the control problem extremely difficult.

A feedback control scheme is implemented as shown in figure 6.1. A lead-lag compensator is included in the feedback signal to the bimorph. The laser displacement signal, with the laser displacement sensor pointed at location 2, is gained and conditioned through the lead-lag compensator to provide the feedback. This lead-lag compensator is designed to counteract a 35º lag at 15 Hz resulting from the displacement signal. Actuator voltage is determined by the value passing through the lead-lag compensator. The voltage input to the bimorph is limited to a maximum output of ± 390 V to avoid damage to the piezo.

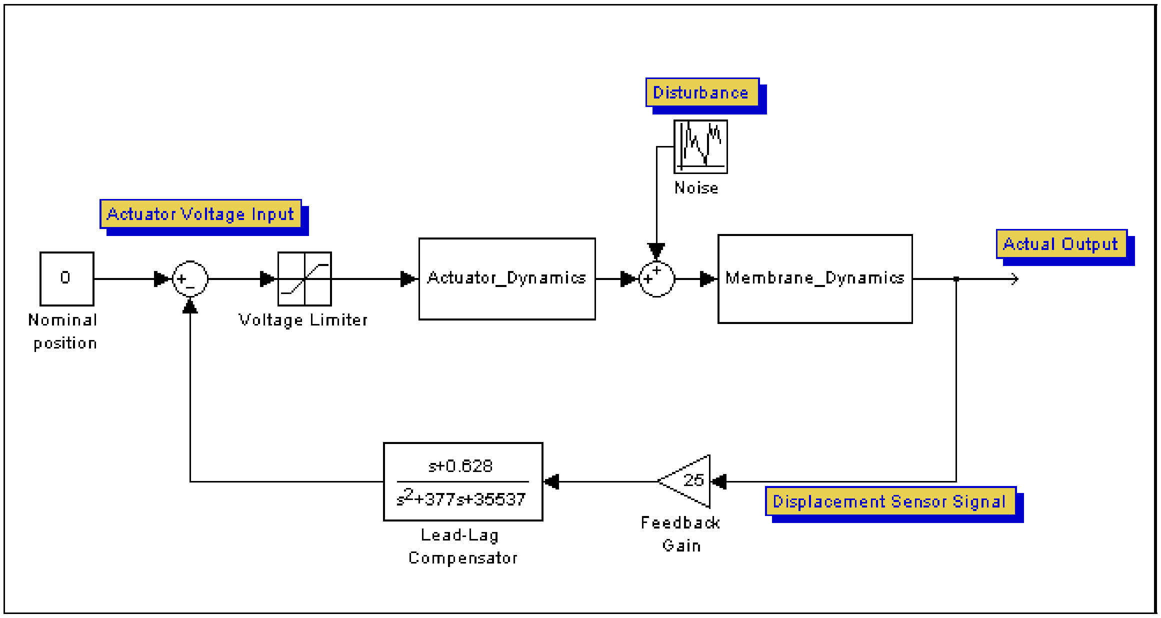

Figure 6.1 Feedback control system configuration

The lead lag compensator transfer function is

$$\frac{\mathbf{S}+0.628}{\mathbf{S}^2+377\,\mathbf{S}+35537} \qquad 6.1$$

and provides a phase lead of 36.6° at 15 Hz, as shown in figure 6.2

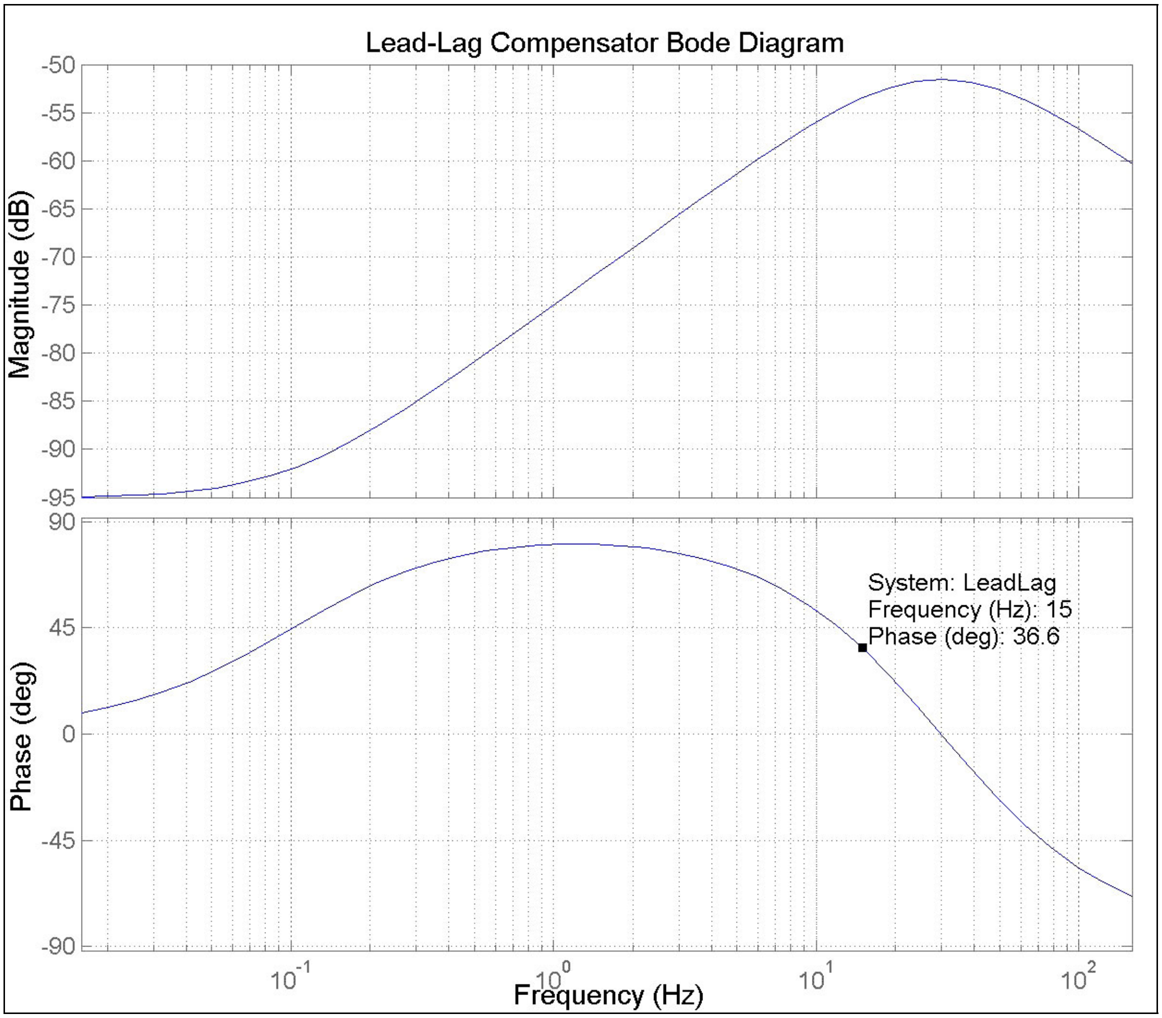

Figure 6.2 Bode diagram of lead-lag compensator used in feedback loop

Control System Results

With the laser displacement sensor pointed to location 2 on the pulley, and an external band-limited disturbance of 50 Hz, the control system is implemented using a dSPACE real-time system. Figure 5.20 shows data without feedback control; with the feedback control, the objective is to decrease the peak magnitude of modes in the targeted frequency range (figure 6.3). One control strategy is to use displacement feedback to decrease the apparent out-of-plane stiffness at the actuator location. This effectively acts as an isolator beyond its resonant frequency. FRF data for the actuator/sensor pair shown in figure 5.19 resembles that of a spring mass system with a fundamental mode around 11 Hz. Since the lead-lag network maintains the phase distortion to a minimum within the same frequency range, the control system will effectively attempt to decrease the resonant frequency of the apparent spring-mass system. Because of the natural high frequency roll-off of the apparent spring mass system, any small change in the resonance frequency is clearly noticeable at high frequencies. The magnitude of the low frequency modes is increased. However, the targeted area shows a decrease in the magnitude of the peaks. This result shows potential for the actuator to execute some disturbance rejection in targeted areas and provide further control.

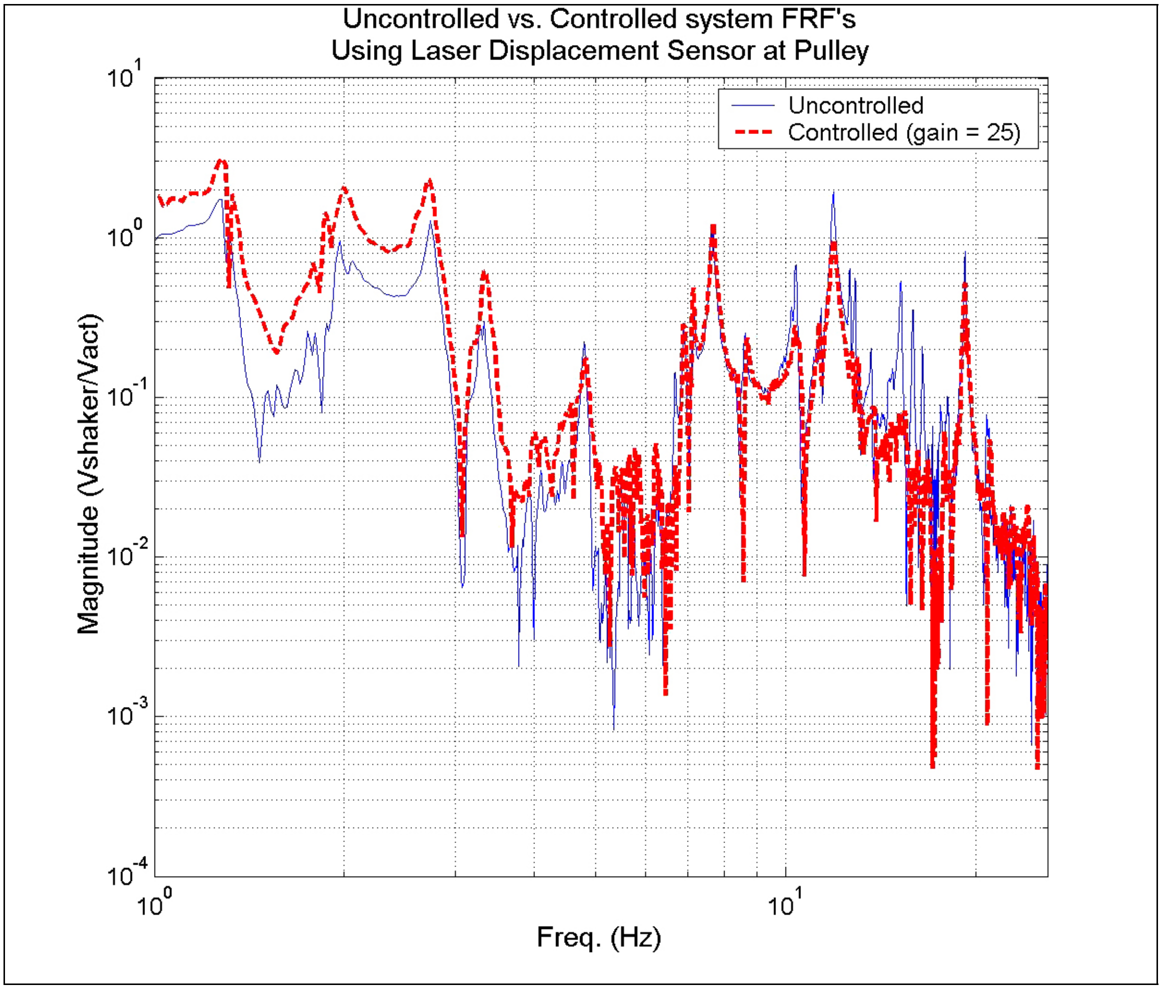

Figure 6.3 FRF of uncontrolled system with controlled system overlaid

FRF data in figure 6.3 show controlled and uncontrolled effectiveness of the actuator as an isolator. Increase or no change in magnitude is observed at frequencies below 10 Hz, but reductions are observed beyond 10 Hz. At high frequencies, the amplitudes when controlled are reduced, indicating isolation. At low frequencies the magnitude is increased, showing the behavior of a typical isolator.

Chapter 7

SUMMARY AND CONCLUSIONS

Summary

A prototype actuator concept has been analyzed, bench tested and utilized to perform vibration disturbance rejection on a large membrane. Despite limitations in dynamic in-plane tension adjustment capabilities, a single actuator has the capacity to provide out of plane excitation to a tensioned membrane. It can be shown that the actuator is capable of exciting the membrane, and therefore it should be able to provide some vibration control or disturbance rejection.

A simplified 2-D model of the actuator provided static and dynamic results for both the in-plane and out-of-plane capabilities of the actuator connected to the membrane. A non-linear dynamics analysis was performed using MATLAB and Simulink and provided a baseline understanding and expectation of the actuator capabilities.

Analytical results provided optimistic expectations for actuator control authority, and bench testing revealed limitations on the actual performance capability of the actuator. Bench testing of in-plane capabilities of the piezo stack actuator proved to be difficult due to inconsistencies in results and variability of multiple parameters. One major source of error between the analysis and experimental results for the stack is friction effects on the pulley, which can be seen in the results of the bench test. This effect increases at higher tension levels, and this may be the reason for some of the discrepancy between analysis and experimentation.

The bench test, however useful, was unable to simulate the boundary conditions for an actuator attached to a tensioned membrane. The in-plane and out-of-plane stiffness of the bench test setup contributed to misleading results. Whereas the bimorph actuator performed poorly under loads greater than 4 lbs (17.79 N) in the bench test setup, it was capable of performing well under tension loads up to approximately 14 lbs (62.27 N) while attached to the membrane.

Testing of a single actuator on the membrane provided reassurance that the actuator would be able to have some control authority on the membrane. Membrane testing also helped to verify issues with membrane tension monitoring and the inability to accurately measure small changes in the membrane tension. A control system was implemented using a single actuator on the membrane, with an external shaker on the torus support structure used for disturbance excitation, and a laser displacement sensor as a local displacement measurement of disturbance of the membrane for feedback. The results show capability for disturbance rejection in the 10 – 20 Hz range, using a lead-lag compensator feedback configuration.

Overall, the insitu performance of the actuator out-of-plane capability is promising with evidence of out-of-plane control authority as well as local disturbance rejection. Global controllability of the entire membrane may not necessarily be assumed from the control system testing results discussed in chapter six, though potential for local control has been shown. Testing of the actuator performance on the membrane was executed using only a single actuator, while the torus has capability for disturbance inputs to the membrane at twelve different locations. Extending the effectiveness of a single actuator into a full set of twelve actuators could produce very positive results in disturbance rejection as well as possibly even global membrane motion control.

Future Work

While the work presented helps to provide a basic understanding of the actuator and the control capabilities of the actuator on a membrane, there is much work that has yet to be done. The issue of in-plane tension adjustment on the membrane is still unresolved, and while the current configuration allows for some tension adjustment, the actual tension of the membrane is not directly measurable. A more reliable method of obtaining and monitoring membrane tension is an area for further consideration.

Known friction problems may possibly be accounted for, but a better understanding of friction levels and effects at various tension levels is necessary in order to incorporate that into the analytical model and account for it in the control system. Further bench testing, and possibly the comparison of frequency response functions from the two load cells may provide sufficient data to obtain a quantifiable friction coefficient, and allow a better understanding of that source of error. Methods of reducing the friction can also be investigated. Other methods of in-plane actuation may be investigated and redesign or further modification of the actuator may be necessary.

Considerably more work needs to be done with the membrane. This includes testing with two actuators on opposite sides of the circular membrane, or three actuators in any number of configurations. Having three actuators ready for testing, a triangular membrane can be placed in the hexapod to replace the circular membrane and testing can show the effectiveness of the actuators on a different shaped membrane.

The controls work done in this paper shows that there is control authority and targeted areas can be controlled. However, more work is needed to optimize the compensator to try to reduce the amplification effects at the lower frequencies, and possibly provide more damping in the targeted areas. Further analysis and curve fitting of the FRF may produce a model that allows for compensator design that has a larger bandwidth and better suppression of the peak magnitudes.

Another area of work involves global measurement of the motion of the membrane, rather than single point measurements, which can only provide local information. The control system that was implemented was capable of controlling a single point on the membrane, though other points were not taken into consideration. While single point control is a step in the right direction, the entire membrane surface must be considered. Global measurements may be possible with videogrammetry, and future research is necessary to incorporate the technology into this application.

BIBLIOGRAPHY

[1] Jenkins, C.H.M.; "Gossamer Spacecraft: Membrane and Inflatable Structures Technology for Space Applications," AIAA, Progress in Astronautics and Aeronautics, Volume 191, 2001.

[2] Chmielewski, A.B., Moore, C., and Howard, R.; "The Gossamer Initiative," IEEE paper 0-7803-5846-5/00, January 2000.

[3] Sausee, M., Park, G., Main J.A., Ruggiero, E., and Inman, D.J.; "Vibration Testing and Analysis of Inflatable Structures using Smart Materials," ASME Adaptive Structures Forum and Material Systems Symposium, New York, NY November 2001, Vol. 3, CD.

[4] Ruggiero, E., Park, G., Inman, D.J., Main, J.A.; "Smart Materials in Inflatable Structure Applications," Proceedings of 43rd AIAA/ASME/ASCE/AHS/ASC Structures, Structural Dynamics, and Materials Conference, AIAA Gossamer Spacecraft Forum, April 22-25, 2002, Denver, CO, in press.

[5] Henson, T.D., Wehlburg, J.C., Redmond, J.M., Main, J.A. and Martin, J.W.; "Thin-Skin Deployable Mirrors for Remote Sensing Systems," Sandia Report SAND2001-0101, January 2001.

[6] Wilkie, W.K., Bryant, R.G., High, J.W., Fox, R.L., Hellbaum, R.F., Jalink, A., Little, B.D., and Mirick, P.H.; "Low-Cost Piezocomposite Actuator for Structural Control

Applications," Proceedings of 7th SPIE International Symposium on Smart Structures and Materials, Newport Beach, CA, March 5-9, 2000.

[7] Williams, B.R., Park, G., Inman, D.J., Wilkie, W.K.; "An Overview of Composite Actuators With Piezoceramic Fibers," Proceedings of IMAC-XX Conference on Structural Dynamics, Los Angeles, CA, Feb 4-7, 2002.

[8] Reaves, M.C., and Horta, L.G.; "Test Cases for Modeling and Validation of Structures with Piezoelectric Actuators," AIAA/ASME/ASCE/AHS/ASC Structures, Structural Dynamics, and Materials Conference and Exhibit, Seattle, WA, April 16-19 2001.

REPORT DOCUMENTATION PAGE	*Form Approved* *OMB No. 0704-0188*

1. REPORT DATE *(DD-MM-YYYY)* 01- 02 - 2005	**2. REPORT TYPE** Contractor Report	**3. DATES COVERED** *(From - To)*

4. TITLE AND SUBTITLE A Prototype Actuator Concept for Membrane Boundary Vibration Control	**5a. CONTRACT NUMBER**
	5b. GRANT NUMBER
	5c. PROGRAM ELEMENT NUMBER
6. AUTHOR(S) Solter, Micah J.	**5d. PROJECT NUMBER** NCC1-01017
	5e. TASK NUMBER
	5f. WORK UNIT NUMBER 23-762-55-MK

7. PERFORMING ORGANIZATION NAME(S) AND ADDRESS(ES) NASA Langley Research Center Hampton, VA 23681-2199	**8. PERFORMING ORGANIZATION REPORT NUMBER**
9. SPONSORING/MONITORING AGENCY NAME(S) AND ADDRESS(ES) National Aeronautics and Space Administration Washington, DC 20546-0001	**10. SPONSOR/MONITOR'S ACRONYM(S)** NASA
	11. SPONSOR/MONITOR'S REPORT NUMBER(S) NASA/CR-2005-213252

12. DISTRIBUTION/AVAILABILITY STATEMENT

Unclassified - Unlimited
Subject Category 39
Availability: NASA CASI (301) 621-0390

13. SUPPLEMENTARY NOTES

The information presented in this report was offered as a thesis in partial fulfillment of the requirements for the degree of Master of Science, The George Washington University in January 2003. Langley Technical Monitor: Lucas G. Horta
An electronic version can be found at http://ntrs.nasa.gov

14. ABSTRACT

In conjunction with the research in ultra-lightweight deployable spacecraft and membrane structures is an underlying need for shape and vibration control. For thin film membrane structures, fundamental modes of vibration for the membrane can be excited through station keeping, attitude adjustments, orbital maneuvers, or contact with space junk or micrometeorites. In order to maintain structural integrity as well as surface shape contour, which may be essential for inflatable antennas, reflective surfaces, or solar sails; vibration damping is a necessary component. This paper discusses development of an actuator attached at the membrane boundary, containing two types of piezoelectric elements, which can be used to perform active control of vibration from the boundary of a membrane. The actuator is designed to control the membrane out-of-plane displacement and in-plane tension by varying the boundary conditions. Results from an initial experimental evaluation of the concept are presented with bench tests of the actuator alone, and with the actuator connected to a large membrane.

15. SUBJECT TERMS

Boundary; Deployable; Membrane; Membrane structures; Shape; Spacecraft; Thin film membrane; Ultra-Lightweight; Vibration; Vibration control

16. SECURITY CLASSIFICATION OF:			**17. LIMITATION OF ABSTRACT**	**18. NUMBER OF PAGES**	**19a. NAME OF RESPONSIBLE PERSON**
a. REPORT	**b. ABSTRACT**	**c. THIS PAGE**			STI Help Desk (email: help@sti.nasa.gov)
					19b. TELEPHONE NUMBER ***(Include area code)***
U	U	U	UU	88	(301) 621-0390

Standard Form 298 (Rev. 8-98)
Prescribed by ANSI Std. Z39.18